HHS Public Access

Author manuscript

Cell. Author manuscript; available in PMC 2025 January 18.

Published in final edited form as:

Cell. 2024 January 18; 187(2): 276–293.e23. doi:10.1016/j.cell.2023.12.003.

Cytoneme Signaling Provides Essential Contributions to Mammalian Tissue Patterning

Eric T. Hall[1], **Miriam E. Dillard**[1], **Elizabeth R. Cleverdon**[1], **Yan Zhang**[1], **Christina A. Daly**[1], **Shariq S. Ansari**[1], **Randall Wakefield**[2], **Daniel P. Stewart**[1], **Shondra M. Pruett-Miller**[1,3], **Alfonso Lavado**[1,4], **Alex F. Carisey**[1], **Amanda Johnson**[2], **Yong-Dong Wang**[1], **Emma Selner**[1], **Michael Tanes**[5], **Young Sang Ryu**[5], **Camenzind G. Robinson**[2], **Jeffrey Steinberg**[5], **Stacey K. Ogden**[1,*,a]

[1]Department of Cell and Molecular Biology, St. Jude Children's Research Hospital, Memphis, TN, 38105, U.S.A.

[2]Cellular Imaging Shared Resource, St. Jude Children's Research Hospital, Memphis, TN, 38105, U.S.A.

[3]Center for Advanced Genome Engineering, St. Jude Children's Research Hospital, Memphis, TN, 38105, U.S.A.

[4]Center for Pediatric Neurological Disease Research, St. Jude Children's Research Hospital, Memphis, TN, 38105, U.S.A.

[5]Center for In Vivo Imaging and Therapy, St. Jude Children's Research Hospital, Memphis, TN, 38105, U.S.A.

Summary

During development, morphogens pattern tissues by instructing cell fate across long distances. Directly visualizing morphogen transport *in situ* has been inaccessible, so the molecular mechanisms ensuring successful morphogen delivery remain unclear. To tackle this longstanding problem, we developed a mouse model for compromised Sonic Hedgehog (SHH) morphogen delivery and discovered that endocytic recycling promotes SHH loading into signaling filopodia

[*]Correspondence: Stacey.Ogden@stjude.org.

Author Contributions

Conceptualization: ETH, ERC, MED, YZ, SKO
Methodology: ETH, ERC, MED, YZ, RW, CGR, CAD, SMP, YDW, DPS, ES, AL, JS
Software: ETH, YW, AFC
Validation: ETH, ERC, DPS
Formal analysis: ETH, YZ, SSA, YDW, JS
Investigation: ETH, ERC, MED, YZ, RW, CAD, DS, YDW, MT, YSR, JS, ES, AJ
Writing: ETH, ERC, MED, YZ, CGM, SMP, SSA, YDW, JS, SKO
Visualization: ETH, ERC, SSA, SKO
Supervision: CGR, SMP, SKO
Funding Acquisition: SKO

[a]Lead Contact: Stacey.Ogden@stjude.org

Declaration of Interests

The authors declare no competing interests.

called cytonemes. We optimized methods to preserve *in vivo* cytonemes for advanced microscopy and show endogenous SHH localized to cytonemes in developing mouse neural tubes. Depletion of SHH from neural tube cytonemes alters neuronal cell fates and compromises neurodevelopment. Mutation of the filopodial motor Myosin 10 (MYO10) reduces cytoneme length and density, which corrupts neuronal signaling activity of both SHH and WNT. Combined, these results demonstrate that cytoneme-based signal transport provides essential contributions to morphogen dispersion during mammalian tissue development and suggest MYO10 is a key regulator of cytoneme function.

Graphical Abstract

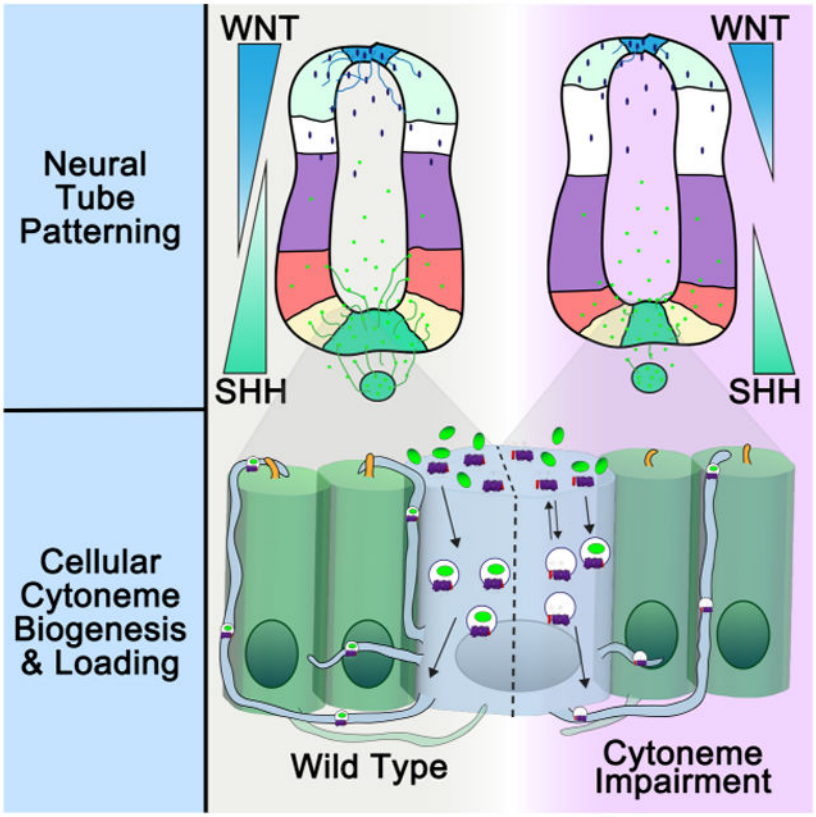

In Brief

During neural tube development, cytonemes, specialized signaling filopodia, contribute to dispersion of Sonic Hedgehog and WNT to ensure appropriate cell fate determination across ventral and dorsal morphogen signaling gradients. Dispatched facilitates endocytic recycling of Sonic Hedgehog to promote ligand entry into cytonemes.

Introduction

Developmental patterning relies on coordinated cell fate decisions that are instructed by signaling proteins called morphogens. Morphogens act in time and concentration-dependent manners to induce distinct cell fates across signaling gradients to pattern complex organs

and tissues [1,2]. Alteration of these gradients leads to developmental disorders and cancers, underscoring the need for precise control of morphogen distribution during development and tissue homeostasis [3].

Proposed models of how morphogens reach their targets include free and assisted diffusion, transcytosis, and direct delivery through specialized filopodia called cytonemes [4]. Experimental evidence supports each dispersion process, but the molecular mechanisms controlling these modes of transport are not clearly defined. The knowledge gap in understanding of how cytonemes influence morphogen signaling has remained disproportionately large because technical challenges often hinder investigation of the structures *in vivo*.

Cytonemes are long, thin, and dynamic cellular extensions that can facilitate direct delivery of Sonic Hedgehog (SHH), WNT, Bone Morphogenic Protein (BMP), growth factors, and NOTCH ligands during development and tissue homeostasis [5-7]. Much of what is known about cytoneme biology stems from investigation of their contributions to *Drosophila* wing disc, air sac primordium, and oocyte organization and development [8-10]. Evidence for cytoneme function during vertebrate development is comparatively limited, but studies using zebrafish, chick, and axolotl models demonstrate that cytonemes impact gastrulation and can promote development and regeneration of the limbs [11-13]. Interrogation of cytonemes in complex organizing tissues like the vertebrate neural tube has remained unfeasible, thus limiting understanding of when and where the structures are active and how they are regulated.

To gain insight into this important biology, we interrogated SHH morphogen signaling[3,14,15]. SHH harbors two covalent lipid modifications including an amino-terminal long chain fatty acid and a carboxyl-terminal cholesterol. Both are essential for SHH signaling gradient establishment and also contribute to regulation of Patched (PTCH) receptors [16-19]. SHH lipids confer high membrane binding propensity to the mature ligand, necessitating specialized machinery that neutralizes lipid tethering for deployment from producing cells. An essential component of this machinery is the twelve-pass transmembrane protein Dispatched (DISP) [20-24]. DISP uses the plasma membrane Na^+ gradient to power SHH membrane extraction for transfer to the extracellular diffusion chaperone SCUBE2 [25-29]. Curiously, genetic studies in mice indicate SCUBE2 may be dispensable for some SHH-regulated developmental processes[30], suggesting independent, redundant, or collaborating deployment mechanisms exist. Accordingly, Hedgehog ligands can localize to vesicular structures inside cytonemes that are released from signaling cells in exosomes [31-36]. Because DISP localizes to cytonemes[36-38], we hypothesized that in addition to facilitating hand off to SCUBE2 for assisted diffusion, DISP also promotes cytoneme-mediated SHH transport. The regulatory mechanisms controlling DISP activity in cytonemes are not yet known.

We previously demonstrated that Furin cleavage in the first extracellular loop of DISP is required for SHH deployment [39]. Structural analyses revealed that although disulfide bonds retain the cleavage fragment after clipping, DISP processing is necessary to open its extracellular domains for SHH release [28,29,40]. To determine how cleavage disruption

impacts SHH cytoneme entry and morphogen gradient activity *in vivo*, we developed a knock-in mouse model of compromised DISP processing (DISP^{CS}). We demonstrate that DISP^{CS} mutant mice have altered neural patterning, cerebellar dysfunction, and high perinatal lethality resulting from depletion of SHH from neuronal cytonemes. Comparable defects in SHH signaling were obtained by disrupting cytoneme function through loss of the actin motor MYO10[36,41]. Notably, WNT signaling, which contributes to dorsal neural tube patterning, was similarly reduced by MYO10 loss. Taken together, our results support that cytonemes play essential roles during mammalian tissue morphogenesis and identify MYO10 as a regulator of cytoneme function.

Results

DISP cleavage is required for neurodevelopment.

CRISPR-Cas9 was used to generate a knock-in mouse with a mutation in the Furin cleavage site in extracellular loop 1 of the *Disp1* gene (Figure S1A)[39]. This resulted in generation of the targeted mutant allele (*Disp1^{CS}*) and an 11 base pair deletion mutant that knocks out gene function (*Disp1^{INDEL}*, Figure S1A). Heterozygous *Disp1$^{CS/+}$* mice were phenotypically normal, while *Disp1$^{CS/CS}$* mutants were runted with variably penetrant hydrocephalus (Figure S1B-C). Thus, *Disp1^{CS}* likely functions as a hypomorphic allele that reduces, but does not ablate, DISP activity. Accordingly, further reducing *Disp1* gene dosage by combining *Disp1^{CS}* and *Disp1^{INDEL}* alleles in *trans* led to highly penetrant and severe phenotypes. Most *Disp1$^{CS/INDEL}$* pups died within one week of birth and surviving animals were runted and failed to thrive (Figure 1A-C, S1D). Surviving *Disp1$^{CS/INDEL}$* mice exhibited hydrocephalus with reduced skull size, narrowed interorbital distances, shortened jaws, and reduced cerebellar volume (Figure 1D-F', S1E-G'), indicative of reduced SHH signaling during development [42-44]. Notably, 97% percent of surviving *Disp1$^{CS/INDEL}$* mice (n=38/39) developed hopping gait ataxia by 6 weeks of age (Figure 1G-I' and Movie 1). Hopping gait can result from depletion of SHH-specified neural progenitors [45,46], suggesting the hopping phenotype is a specific manifestation of reduced SHH signaling in *Disp1$^{CS/INDEL}$* animals, and not a general ataxia resulting from cerebellar dysfunction.

To investigate how tissue patterning was impacted in *Disp1$^{CS/INDEL}$* mice across a SHH morphogen gradient, we analyzed developing neural tubes of E9.5/25-30 somite embryos. Beginning around ~E8.0, SHH from the notochord signals to induce the neural tube floor plate, which is marked by FOXA2. SHH also specifies distinct ventral neural tube progenitor domains marked by NKX2.2, OLIG2, and PAX6 [47]. Induction of these ventral cell fates is highly sensitive to fluctuations in SHH exposure, so progenitor domain establishment can be used as a readout for SHH morphogen gradient activity [48,49]. Published studies demonstrate that mice with heterozygous *Disp1* mutation are phenotypically indistinguishable from wild type animals while complete loss of DISP activity leads to death by E9.5 [21-23]. Accordingly, *Disp1$^{CS/+}$* and *Disp1$^{INDEL/+}$* embryos appeared phenotypically normal with stereotypical neural tube progenitor domain establishment (Figure 2A-C, F-H, K-N). Conversely, *Disp1$^{INDEL/INDEL}$* mutants, which lack a functional *Disp1* allele, die around E9.5 with neural tube defects including complete ventralization of PAX6 and loss of the FOXA2, NKX2.2, and OLIG2 progenitor domains (Figure 2D, I, K-N). *Disp1$^{CS/INDEL}$* neural tubes

retained sufficient SHH signaling activity to induce the floor plate and NKX2.2 and OLIG2 progenitor domains. However, the domains were reduced in size and shifted ventrally compared to control (Figure 2J compared to 2F, K-Q and S2A-A'). Accordingly, RNAscope *in situ* hybridization analysis revealed reduction in the *Gli1* expressing cell population in *Disp1*$^{CS/INDEL}$ embryos compared to controls (Figures 2R-W and S2B-C). RNAseq analysis confirmed that neuronal differentiation was compromised in *Disp1*$^{CS/INDEL}$ embryos (Figure S2D-G). Thus, DISP cleavage is required for proper SHH morphogen gradient activity during neurodevelopment.

DISP endocytosis is altered by cleavage disruption.

In *Drosophila*, deployment of Hh from polarized epithelial cells requires Disp-mediated internalization and endocytic recycling [37,50]. To test whether DISP recycling occurred in mammalian cells, we developed an *in vitro* system to interrogate DISP trafficking in polarized, multicellular spheroids. Murine inner medullary collecting duct (IMCD3) cells, which are polarized and can form multicellular spheroids in 3D culture [51], were transduced with vectors encoding WT or CS V5-DISP-HA proteins and doxycycline-inducible SHH (Figure 3A-G, S3A-A'). IMCD3 cells were cultured in Matrigel to promote their organization into spheroids with apical lumens (Figure 3A-E). Signal overlap between V5 and HA epitope tags was used to track uncleaved DISP^{CS} and processed DISP^{WT} with its disulfide bond tethered amino-terminus [28,29]. Without SHH, DISP^{WT} localized more basally while DISP^{CS} distributed uniformly along cellular membranes (Figure 3A', C'). Following doxycycline induction, SHH accumulated in the apical lumen and along cellular membranes and DISP^{WT} enriched uniformly along basolateral membranes (Figure 3B' and F-G). DISP^{CS} apicobasal distribution did not change following SHH induction (Figure 3D' and F-G), suggesting Furin cleavage primes DISP for SHH-stimulated membrane redistribution in polarized epithelial cells.

To determine the molecular mechanism by which SHH-stimulated DISP membrane redistribution occurs, we stably expressed V5-DISP-HA proteins in *Disp1*$^{-/-}$ (*Disp*^{KO}) mouse embryonic fibroblasts (MEF). This allowed examination of DISP membrane trafficking in a background devoid of endogenous DISP protein that might influence DISP^{CS} recycling through oligomeric association [39,52]. Cell surface biotinylation and cycloheximide treatment experiments confirmed DISP^{WT} and DISP^{CS} proteins had similar cell surface expression and degradation kinetics, indicating cleavage disruption does not significantly reduce DISP protein stability or limit its membrane access (Figure S3B-C', N). To probe SHH-induced changes in DISP membrane recycling, we performed immunofluorescence colocalization analyses and calculated Pearson's correlation coefficients between DISP and endocytic marker proteins Adaptor Protein 2α (AP2), clathrin, caveolin, Rab4, Rab5, Rab7, and Rab11 (Figure 3H-H')[53]. Whereas DISP^{WT} and DISP^{CS} proteins showed similar colocalization levels with the clathrin adaptor protein AP2 in the absence of SHH, differences emerged upon SHH expression. In cells expressing SHH, DISP^{WT} colocalization with AP2 increased while DISP^{CS}-AP2 colocalization remained unchanged (Figure 3H', S3D-G). SHH-induced colocalization increases were also observed between DISP^{WT} and clathrin, Rab4, Rab5, Rab7, and Rab11 (Figures 3H' and S3H-M), suggesting DISP^{WT} interaction with SHH enhances endocytic recycling. DISP^{CS} enrichment in recycling

endosomes did not increase in response to ligand. However, it was slightly more enriched than DISP^{WT} in clathrin, Rab5, Rab7, and Rab11-marked endocytic compartments in the absence of SHH (Figures 3H' and S3H-M).

DISP colocalization with caveolin was unaltered by either cleavage site mutation or SHH expression, suggesting clathrin-mediated endocytosis is the primary route for SHH-stimulated DISP endocytic recycling (Figure 3H'). Accordingly, we identified four putative dileucine binding motifs for the AP2 clathrin adaptor complex in the intracellular carboxyl-terminal tail of DISP (Figure 3I). To determine whether these motifs contributed to SHH-stimulated recycling, we generated a carboxyl-terminal deletion mutant lacking all four motifs (DISP$^{\Delta C}$) and a mutant in which the four motifs are mutated to alanine (DISP^{4xAA}). Both DISP$^{\Delta C}$ and DISP^{4xAA} reached the cell surface and were effectively processed by Furin, as demonstrated by cell surface biotinylation and V5 cleavage fragment production (Figure S3N). Importantly, both ΔC and 4xAA mutants showed higher enrichment in biotinylated plasma membrane fractions than DISP^{WT} and DISP^{CS}, consistent with the AP2 binding sites contributing to DISP endocytosis (Figure S3N). DISP$^{\Delta C}$ plasma membrane enrichment was more pronounced than that of DISP^{4xAA}, suggesting an additional motif in the carboxyl-terminal fragment may contribute to membrane internalization. Thus, we focused on DISP$^{\Delta C}$ for further analysis. Likely due to the modestly elevated baseline colocalization observed between DISP^{CS} and endocytic machinery, DISP^{CS} showed lower cell surface localization than DISP^{WT} (Figure 3H' and S3N).

To further probe this mechanism, we tested whether Furin cleavage impacted DISP-AP2 binding. V5-DISP-HA proteins were expressed in SHH-expressing *Disp*^{KO} MEFs and coimmunoprecipitation experiments were performed. Consistent with DISP internalizing through a clathrin/AP2-dependent mechanism, both α and β-Adaptin proteins were present in anti-HA coimmunoprecipitates with DISP^{WT} (Figure 3J, lane 5). AP2 adaptor subunits were reduced in both V5-DISP^{CS}-HA and V5-DISP$^{\Delta C}$-HA coimmunoprecipitates (Figure 3J, lanes 6-7), supporting that DISP binds AP2 through one or more of the identified carboxyl-terminal binding motifs and that Furin cleavage enhances DISP-AP2 association through these sites following SHH binding.

To test whether reduced AP2 binding altered DISP^{CS} or DISP$^{\Delta C}$ internalization kinetics, we tagged wild type and mutant DISP proteins with the photostable fluorescent tag Dronpa3 [54] and tracked baseline and SHH-stimulated internalization in Madin-Darby canine kidney (MDCK) cells[52,55]. To accurately track membrane internalization, we first paused endocytosis by using the clathrin inhibitor Pitstop 2 [56], and then monitored DISP-Dronpa3 plasma membrane signal intensity before and after Pitstop 2 washout (Figure 3K-L'). Consistent with clathrin being the primary route by which DISP internalizes, all DISP variants accumulated on the plasma membrane in response to Pitstop 2 (Figure 3K and L). Following Pitstop 2 washout, membrane signal intensity of all three DISP proteins decreased but differences were evident in their internalization rates (Figure 3K' and L'). As per the modestly elevated colocalization observed between DISP^{CS} and endocytic markers that did not change in response to SHH (Figure 3H'), DISP^{CS} internalized at a constant rate in both the absence and presence of ligand. Conversely, SHH expression accelerated DISP^{WT} internalization to a rate faster than that of DISP^{CS} (Figure 3K'), further suggesting

the wild type protein undergoes ligand-stimulated endocytosis. DISP$^{\Delta C}$ internalized more slowly than DISP^{WT} in both the absence and presence of SHH, confirming that the carboxyl-terminal AP2 binding motifs are necessary for efficient DISP endocytosis (Figure 3L'). Taken together with the experiments above, these results suggest DISP membrane recycling occurs through clathrin-mediated endocytosis, and that Furin cleavage enhances DISP responsiveness to SHH for ligand-stimulated recycling endocytosis (Figure 3M).

DISP mutation reduces SHH cytoneme entry.

Studies in flies and vertebrates indicate that Hh ligands are released from producing cells in exovesicles and previous work from our lab showed localization of SHH and DISP to vesicles inside cytonemes [31-33,35,36]. Thus, we hypothesized endocytic recycling of DISP-SHH complexes might facilitate SHH vesicular enrichment for cytoneme entry. To test whether attenuated endocytic recycling activity of DISP^{CS} altered the amount of SHH in cytonemes, we stably expressed WT or CS V5-DISP-HA proteins in *Disp^{KO}* MEFs and then quantified cytoneme occurrence rates and SHH and DISP cytoneme entry (Figure 4). We previously demonstrated that SHH coreceptors BOC and CDON promote cytoneme occurrence in SHH-producing cells, and that DISP is not required for cytoneme formation in cultured mouse fibroblasts [36]. Accordingly, SHH expression increased cytoneme occurrence rates independent of DISP (Figure 4A). Despite its ability to promote cytoneme occurrence in *Disp^{KO}* cells, SHH failed to efficiently enter cytonemes of cells lacking DISP protein or to activate signaling in SHH Light II *Gli-luciferase* reporter cells co-cultured with SHH-producing *Disp^{KO}* MEFs (Figure 4B, E, S3O). Expression of DISP proteins in *Disp*^{KO} MEFs revealed that DISP^{WT} and DISP^{CS} entered cytonemes with similar efficiencies. Despite this, only DISP^{WT} significantly increased SHH cytoneme entry, albeit to a level slightly lower than what is observed in wild type cells (Figure 4B-G'). Similarly, DISP^{WT} expressed in SHH-producing cells showed greater signaling activity in the SHH Light II cell co-culture assay than DISP^{CS} (Figure S3O). Thus, ligand-stimulated endocytic recycling of DISP-SHH complexes may facilitate SHH packaging into vesicles for cytoneme loading and/or signaling.

To further assess the impact of reduced SHH cytoneme entry in DISP^{CS} expressing signal producing cells on pathway induction in receiving cells, we monitored SHH-activated Ca^{2+} flux [36]. *Disp^{KO}* MEFs expressing SHH alone or with WT or CS DISP proteins were co-cultured with Ca^{2+} reporter cells and flux rates were quantified in cytoneme-contacted reporter cells. Ca^{2+} flux rates correlated with SHH cytoneme loading status such that DISP^{WT}-expressing cells induced significantly higher flux rates than *Disp^{KO}* or DISP^{CS}-expressing cells (Figure 4H). Thus, the DISP^{CS} mutation, which compromises SHH-stimulated DISP endocytic recycling, attenuates its ability to chaperone SHH into cytonemes that contribute to contact-mediated signaling.

SHH-containing cytonemes are present in the neural tube.

We developed tissue processing, fixation, and imaging strategies to allow for preservation and detection of cytonemes in developing mouse tissue [57]. Using these methods, we searched for cytoneme-like extensions reaching from SHH-producing notochords and neural tube floor plates. A *Shh-Cre;membrane-Tomato/membrane-GFP (mT/mG)* reporter was

used to mark *Shh*-expressing cell membranes with GFP [58,59]. Confocal microscopy of cardiac level sections from E9.5/25-30 somite embryos revealed GFP-positive membrane extensions stretching from cells of the floor plate towards neighboring, non-GFP expressing cells. These extensions were observed in 88% of the tissue sections analyzed (Figure 5A, arrows). GFP-positive floor plate extensions were also observed reaching across the neural tube lumen to contact neighboring non-GFP labeled cells (Figure 5B-B'). On average, ~11 lumen extensions were observed per tissue section analyzed, suggesting that SHH-producing cells of the developing neural tube can directly contact target cell populations.

To determine whether the neural tube extensions were cytonemes, we tested for localization of SHH and actin. We validated anti-SHH antibody staining in neural tube sections using a Shh^{GFP} knock-in allele that generates an internally GFP labeled, lipid modified SHH protein from the endogenous *Shh* promoter [60]. $Shh^{+/+}$, $Shh^{GFP/+}$, $Shh^{GFP/GFP}$ embryos were stained using anti-GFP and anti-SHH and then analyzed by confocal microscopy. Whereas $Shh^{+/+}$ embryos showed negligible colocalization between anti-GFP and anti-SHH signals, signal overlap in the notochord and floor plate increased with increasing Shh^{GFP} allele zygosity (Figure S4A-C). Because the SHH antibody showed sufficient sensitivity to detect SHH protein in fixed tissue samples, we tested whether floor plate-derived extensions contained endogenous SHH and actin by whole mount immunostaining of wild type embryos (Figure 5C). Actin-positive extensions that contained SHH puncta were detected reaching from the floor plate into the neural tube lumen, suggesting GFP-labeled membrane extensions observed in neural tube lumens of *Shh-Cre;* $Rosa26^{mT/mG}$ embryos were likely cytonemes (Figure 5B-C').

To investigate trajectories of neural tube cytonemes, scanning electron microscopy (SEM) was performed on sagittally bisected E9.5 $Disp1^{+/+}$, $Disp1^{INDEL/+}$ and $Disp1^{INDEL/INDEL}$ embryos that were processed to expose the notochord, floor plate, and apical surfaces of cells lining the neural tube lumen (Figures 5D and S4D). Long, thin cellular extensions were observed reaching across apical membranes of cells lining the lumen and contacting apical primary cilia of adjacent cells in both control and $Disp1^{INDEL/INDEL}$ embryos (Figure 5E-H). Approximately 50% of apical primary cilia were contacted by an extension independent of DISP status, suggesting functional significance for these associations (Figure 5H-I). Whereas the majority of cellular connections contacted apical membranes of cells lining the neural tube lumen, tip-to-tip connections suggestive of morphogenetic synapses akin to those proposed to function in *Drosophila* were also observed [61] (Figure 5F, green circle). Due to the complex architecture of the neural tube, it was difficult to identify cells of origin for most extensions. However, extensions often appeared to enter the lumen at sites of cell-cell contact (Figure S4E, green arrow). Accordingly, extensions originating from cells of the ventral floor plate could be tracked into the neural tube lumen, suggesting they may pass between cell-cell junctions (Figure S4F-G, green arrows). Consistent with *in vitro* experiments demonstrating that DISP is not required for cytoneme formation, neural tube extensions had similar apically exposed lengths and occurrence rates in all genotypes examined (Figures 5G and S4H). Notably, cellular extensions from all genotypes displayed bulges along their lengths that could represent vesicular cargo (Figure S4F-G, yellow arrows), as previously reported for *Drosophila* and murine cell culture [36,62].

Cytoneme-based apical SHH delivery.

Primary cilia function as signaling hubs that are enriched for SHH pathway components including the receptor PTCH, signal transducer Smoothened (SMO), and GLI transcriptional effectors [63,64]. Thus, apical cytoneme delivery of SHH to primary cilia would be an efficient mechanism for rapid pathway activation. Because SHH specification of ventral neural tube progenitor domains occurs between E8.5-E9.0/8-20 somites[47], 17-20 somite stage wild type embryos were examined by confocal microscopy to probe for SHH near primary cilia of cells lining the neural tube lumen. We observed SHH inside the lumen where it frequently colocalized with ARL13B-marked primary cilia (Figure 5J, arrowheads). Notably, 46% (n=39/84) of actin-positive extensions from the floor plate that contacted ARL13B-marked apical primary cilia in adjacent cellular populations contained SHH (Figures 5K-K", S4I-J" and Movies 2-3). These results, which are consistent with a previous report demonstrating SHH near cilia[60], suggest cytonemes can directly deliver SHH to ciliary PTCH receptors.

To test whether cytoneme-like extensions from *Shh*-expressing cells inside the floor plate could enter the neural tube to deliver SHH into the apical lumen, we performed serial block face SEM (SBF-SEM) on neural tubes of control and DISP mutant E9.5 embryos (Figure 5L-M, S4K-M). Multiple membranous 'blebs' were present between cells in individual segments in all genotypes tested (Figure 5L, S4K', L'). When mapped through sequential scans to generate a volumetric 3D reconstruction, the blebs connected to reveal long contiguous extensions tracking toward the lumen (Figures 5M and S4M, Movie 4). Although high cell density in the floor plate prevented us from mapping these extensions into the lumen, similarities in size and trajectory to cytonemes observed in confocal and SEM images of sagittal neural tube sections suggests they are similar structures (Figures 5A-C', arrows and S4F-G, black arrows). As such, we propose cytonemes traverse the ventral neural tube to facilitate SHH delivery to the apical lumen.

DISP increases SHH entry into neuronal cytonemes.

SHH from the notochord is crucial for induction of the floor plate, signaling to the somites, and organization of the surrounding mesenchyme [65-69]. Accordingly, SEM of the notochord and surrounding tissue revealed interactions between membrane extensions from cells of the notochord, floor plate, and mesenchyme in both control and DISP mutant embryos (Figures 6A, C-E, S5A-B, Movie 5). Confocal imaging of E8.5 *Shh-Cre; Rosa26*$^{mT/mG}$ and E9.5 *Shh*$^{GFP/+}$ embryos confirmed the extensions to be SHH, F-actin, and GFP-positive, suggesting they are cytonemes (Figure 6B-B", S5C-C'"). Notably, E8.5 *Shh-Cre; Rosa26*$^{mT/mG}$ embryos revealed GFP-labeled notochord extensions reaching toward SHH-responsive somites[69] (Figure S5C-C'"). These results suggest that the extensions may facilitate communication between the notochord and surrounding cellular populations.

To determine whether DISP was required for localization of SHH to notochord-derived cytonemes, *Shh*^{GFP} was introduced into control and *Disp1* mutant backgrounds, and notochord to floor plate connections were examined by confocal microscopy. Multiple F-actin-positive extensions reached from the notochord to the floor plate and mesenchyme in all genotypes examined (Figure S5D-G). Remarkably, SHH was present in cytonemes between the notochord, floor plate, and mesenchyme in control embryos, but depleted from

cytonemes of *Disp1*$^{INDEL/INDEL}$ and *Disp1*$^{CS/INDEL}$ embryos (Figure 6F-L). We quantified the number of SHH puncta per notochord-derived cytoneme in E9.5 *Disp1*$^{INDEL/+}$, *Disp1*$^{INDEL/INDEL}$, and *Disp1*$^{CS/INDEL}$ embryos using both manual and automated methods. We found that cytonemes of DISP mutant genotypes had significantly fewer SHH puncta than control embryo cytonemes (Figures 6J-L and S5H-I). Consistent with these connections being necessary for transport of notochord-derived SHH to induce signaling in the floor plate, SHH protein levels were significantly reduced in floor plates of *Disp1*$^{INDEL/INDEL}$ embryos (Figure 6H-I). Notochord-derived SHH was detected along basal membranes of floor plate cells in both control and *Disp1*$^{INDEL/INDEL}$ mutant embryos, indicating basal signal can still accumulate when cytoneme-based transport is compromised (Figure 6H-I, arrows). Despite this accumulation, SHH was not detected inside the floor plate in embryos lacking DISP activity, suggesting basal membrane ligand accumulation is not sufficient for robust induction of high-threshold target genes. Based upon our *in vitro* and *in vivo* results, we propose DISP facilitates endocytic recycling of SHH to load ligand into cytonemes for apical morphogen delivery that contributes to neural tube patterning (Figure 6M).

Myosin 10 promotes cytoneme signaling.

The actin motor MYO10 promotes filopodial formation and our *in vitro* studies revealed that it contributes to cytoneme-mediated SHH transport in cultured cells [36,41,70]. Accordingly, we previously demonstrated that loss of MYO10 *in vivo* disrupts SHH signaling in the developing neural tube [36]. To probe whether this phenotype resulted from alteration of cytoneme formation, we used our cytoneme-optimized tissue processing protocol to visualize cytonemes in *Myo10*$^{m1J/m1J}$ mice [71]. We began by analyzing E8.5 embryos, a stage where SHH expression is significantly higher in the notochord than in the floor plate [60]. At this stage, memGFP signal was restricted to the notochord of E8.5 *Shh-Cre; Rosa26*^{mTmG} embryos (Figure 7A-B', E-F). Whereas numerous extensions were visible along the notochord of control embryos, few were detected along notochords of *Myo10*$^{m1J/m1J}$ embryos (Figure 7A-B'), suggesting a role for the actin motor in their formation.

To quantify lengths and occurrence rates of neural tube extensions in control and *Myo10*$^{m1J/m1J}$ embryos, SBF-SEM datasets of E9.5 embryos were annotated using CATMAID software [72].

This revealed that *Myo10*$^{m1J/m1J}$ neural tubes had fewer extensions than control, and that average lengths of existing extensions were comparatively shorter (Figure 7C-D, S6A-E, and Movie 6). This depletion correlated with altered *Olig2* expression patterns ranging from complete loss to a pronounced ventral shift of OLIG2 in *Myo10*$^{m1J/m1J}$ E8.5/10-13 somite embryos (Figure 7A' vs. B', E-G). This shift is indicative of a reduction in high-level SHH signaling that normally restricts *Olig2* from the cells directly adjacent to the floor plate [47,73]. Similarly altered *Olig2* expression patterns were observed in *Disp1*$^{CS/INDEL}$ embryos at E8.5/10-13 somites, supporting that comparable functional defects are triggered by either reducing cytoneme density (*Myo10*$^{m1J/m1J}$) or depleting SHH from them (*Disp1*$^{CS/INDEL}$) (Figure S6F-H). Consistent with MYO10-promoted cytonemes contributing to SHH transport during the early stages of ventral cell fate determination, SHH

signal was depleted from the neural tube lumen of E8.5 *Myo10*$^{m1J/m1J}$ embryos (Figure 7E" compared to F", H-I). Thus, we propose MYO10 is an essential modulator of cytoneme function and SHH signaling *in vivo*.

During dorsal neural tube patterning, WNT and BMP proteins produced at the roof plate signal in opposition to notochord and floor plate-derived SHH [74-76]. Consistent with previous reports that both WNT and BMP family members transport along cytonemes [13,77], we observed actin-positive extensions reaching from the roof plate into the dorsal neural tube lumen (Figure S6I). To query whether dorsal cytonemes may contribute to transport of WNT and/or BMP in the neural tube, we first performed *in vitro* cytoneme occurrence assays to determine whether MYO10 impacts WNT or BMP cytoneme formation. We quantified cytoneme occurrence rates in control and *Myo10*$^{-/-}$ MEFs in the absence or presence of SHH-GFP, BMP2-GFP, BMP4-OFP, BMP7-GFP, and WNT1-GFP [36]. Whereas BMP2, 4, or 7 fluorescent protein expression did not significantly alter cytoneme occurrence rates, both SHH-GFP and WNT1-GFP increased occurrence in a statistically significant manner in wild type MEFs (Figure S6J, light gray). Neither SHH-GFP nor WNT1-GFP increased cytoneme occurrence in *Myo10*$^{-/-}$ cells, supporting that, in addition to contributing to SHH cytoneme formation, MYO10 is also a modulator of WNT cytoneme formation (Figure S6J, dark gray).

To assess the impact of MYO10 loss on neural tube WNT signaling *in vivo*, control and *Myo10*$^{m1J/m1J}$ E9.5/25-30 somite embryos were examined to assess expression of the WNT target *Olig3*. The dorsal expression domain of OLIG3 was reduced by MYO10 loss (Figure 7J-M). Consistent with *in vitro* results that loss of MYO10 does not impact cytonemes of BMP-expressing cells, dorsal enrichment of BMP-induced phospho-SMAD (pSMAD) was unaffected in *Myo10*$^{m1J/m1J}$ neural tubes (Figures 7N-Q and S6J). Notably, RNAseq analysis of E8.5 *Myo10*$^{+/+}$ and *Myo10*$^{m1J/m1J}$ embryos revealed that both SHH and WNT pathways were attenuated and that BMP signaling was not significantly altered following MYO10 loss (Figure S7). Intriguingly, NOTCH signaling, which can occur through context-dependent cytoneme transport[7], was also identified as being reduced in *Myo10*$^{m1J/m1J}$ embryos (Figure S7D, D"). Taken together with the above, these results suggest MYO10 is a general modulator of cytoneme function and that, in addition to diffusion-based mechanisms of signal dispersion, cytoneme-based transport contributes to WNT and SHH-mediated patterning of the developing neural tube.

Discussion

Dispatched cleavage promotes SHH-stimulated endocytic recycling.

Since our initial report highlighting the importance of DISP cleavage for SHH deployment, multiple DISP structures have been solved [28,29,39,40,78]. Structural evidence suggests the cleavage fragment remains tethered but that clipping opens the extracellular domain of DISP to accommodate SHH binding [28,29,40,78]. Our new cell biological experiments show that DISP cleavage enhances responsiveness to SHH-stimulated AP2-dependent endocytic recycling. Thus, we propose DISP cleavage stabilizes a protein conformation that shifts to "open" the intracellular tail for robust AP2 binding upon SHH engagement (Figure 3M). We speculate Furin cleavage disruption alters DISP conformation such that it interacts

with AP2 at an intermediate affinity for constitutive midlevel endocytic recycling. Because the intracellular domains of DISP failed to resolve in vertebrate DISP cryo-EM structures [28,29,40], we cannot unequivocally conclude that SHH induces conformation changes that impact the AP2 binding sites. Nevertheless, cell biological assays reveal a key functional difference between $DISP^{WT}$ and $DISP^{CS}$ proteins is the ability of $DISP^{WT}$ to undergo enhanced recycling with SHH in signal-producing cells.

Cytonemes transport morphogens during neural tube patterning.

In mice, notochord-derived SHH signals to the ventral neural tube to begin instructing ventral fates around E8.0. By E9.5, *Shh* expression is induced in the floor plate, which serves as a secondary source of SHH for the neural tube after the notochord begins to regress [60]. Most ventral fates are established by E8.5, suggesting initial patterning information is conveyed through notochord-derived signal [60,66]. However, mechanisms by which lipid-modified SHH travels from the notochord, across the floor plate, and into the apical neural tube have remained undefined. Development of optimized tissue processing and imaging protocols for visualizing long filopodia in embryonic mouse tissue allowed us to test the hypothesis that cytonemes contribute to this transport. We observed SHH in cytonemes from the notochord and floor plate and propose the filopodia are conduits that help move SHH during establishment of the signaling gradient (Figure 7R). Consistent with this hypothesis, loss of the filopodial actin motor MYO10 reduces formation of notochord and floor plate extensions and disrupts SHH signaling in the ventral neural tube. Notably, genetic and RNAseq data indicate that MYO10 mutants have reduced signaling by additional cytoneme cargo proteins WNT and NOTCH, suggestive of a general role for MYO10 in facilitating cytoneme-based morphogen transport. Such functionality provides a potential explanation for neural phenotypes of $Myo10^{m1J/m1J}$ mice ranging from compression of the SHH signaling gradient to severe exencephaly, which can result from corruption of WNT pathway activity [36,71,79].

Cytonemes contribute to apical SHH delivery.

Despite experimental support for an apical SHH signaling gradient in vertebrate neural tubes, the question of whether Hedgehog signals are received by polarized epithelial cells apically or basally remains a topic of fervent debate [32,35,37,50]. Most studies performed in *Drosophila* wing disc epithelia, which lack primary cilia, suggest long range Hh signals accumulate basally [31,32,37]. In zebrafish, SHH accumulates on basal membranes of cells in the developing optic cup that over-express the SHH co-receptor CDON [80]. However, in mice SHH is only detectable on basolateral membranes of signal-receiving cells at later developmental stages after initial patterning information has been conveyed and *Shh* expression has been induced in the floor plate [60]. Our investigation of neural tube SHH distribution revealed notochord-derived ligand along basal membranes of floor plate cells in E8.5 and E9.5 embryos, but this signal did not effectively induce the floor plate in DISP mutants. This is likely because, in vertebrates, apical primary cilia are the key sites of SHH pathway control [81]. PTCH on ciliary membranes regulates ciliary SMO by limiting membrane accumulation of SMO-activating sterols [82-85]. This makes the ciliary localized pool of PTCH the essential fraction to which SHH must gain access to rapidly activate SMO. Thus, we favor a model in which SHH is received apically by neuroepithelia

to activate signaling during morphogen gradient establishment. We speculate basolateral accumulation of SHH contributes to refinement or reinforcement of ventral cell fates at later developmental stages by sequestering PTCH away from ciliary SMO during neural tube maturation. Such reinforcement is likely necessary because target cell responses to the SHH gradient remain dynamic throughout ventral neural tube patterning [66].

We anticipate that in addition to facilitating notochord to floor plate communication, cytonemes also promote communication between the notochord and mesenchyme for formation of the nuclei pulposi of intervertebral discs [67,68]. Accordingly, we observed notochord-derived SHH-containing extensions contacting neighboring mesenchymal cells and reaching toward somites. These results suggest that cytonemes extend from developmental organizing centers to facilitate simultaneous communication with multiple responding cell populations for coordination of multi-tissue patterning during early development.

Direct delivery vs. diffusion.

If SHH-producing cells use cytonemes to deliver morphogens to responding cells, what role does diffusion play and what is the specific role of the extracellular SHH chaperone SCUBE2? Biochemical and genetic studies suggest SCUBE2 shields SHH lipid modifications from the extracellular environment for chaperone assisted diffusion [26,27]. However, neurodevelopment is not reported to be compromised in *Scube2*$^{-/-}$ mice [30], indicating that redundancies with other SHH transport mechanisms exist. We hypothesize cytonemes may provide this redundant and/or cooperating transport functionality, as is suggested by differing requirements for the DISP intracellular tail for these distinct transport mechanisms. The results presented here demonstrate the carboxyl-terminal tail is essential for SHH endocytic recycling and cytoneme entry. Conversely, published work indicates the tail is dispensable for DISP mediated SHH transfer to SCUBE2 [28]. Thus, cooperative and/or compensatory activity may occur between diffusion and cytoneme-based transport processes to ensure appropriate signal dispersion during development.

Limitations of the Study

The imaging protocols optimized for this study represent a significant technical advance towards visualization of morphogen transport across developing tissues *in situ*. However, technical limitations stemming from tissue depth, size, and organization of the neural tube currently preclude us from performing correlative light electron microscopy or monitoring SHH transport from the notochord and neural tube through cytonemes by live imaging in tissues. As such, we do not yet know how *in vivo* cytonemes connect, how stable they are, whether they pass through tight junctions to gain access to apical cilia, how far they track across the SHH signaling gradient, and if their lengths correlate with gradient steps. Future studies will be focused on enhancing tissue processing and protein labeling to optimize challenging imaging experiments that can be used to generate high resolution maps of cytoneme communication networks across developing embryos.

STAR Methods

RESOURCE AVAILABILITY

Lead contact—Further information and requests for resources and reagents should be directed to the lead contact, Stacey Ogden (stacey.ogden@stjude.org).

Materials availability—Reagents generated in this study are available upon request pursuant to completion of an institutional material transfer agreement. Protein expression vectors will be deposited at Addgene.

Data and code availability

- Bulk RNA sequencing data have been deposited in the Gene Expression Omnibus and are publicly available at https://www.ncbi.nlm.nih.gov/geo/query/acc.cgi under Accession number GSE242161 as listed in the key resources table. All data reported in this paper will be shared by the Lead Contact upon request.
- This paper does not report original code.
- Any additional information required to reanalyze the data reported in this work paper is available from the Lead Contact upon request.

EXPERIMENTAL MODEL AND STUDY PARTICIPANT DETAILS

Mice—The mouse experiments in this study were conducted under protocols approved by the Institutional Animal Care and Use Committee (IACUC) of St. Jude Children's Research Hospital (protocol 608-100616). The St. Jude Institutional Animal Care and Use Committee approved all procedures in accordance with the Guide for the Care and Use of Animals. Mice were housed in accordance with IACUC standards in barrier conditions with micro-isolation cages to minimize pathogen exposure. The mouse housing facility operates on a 12-12 automated light system (12 hours light on, 12 hours light off) with an isolated ventilation system. Mice were fed standard chow and provided water ad libitum. The analyses performed in these studies showed no difference between genders aside from animal weights which have been analyzed separately by sex and compared to genotypes of interest. Both male and female specimens are included equally in our analyses. Complete information on developmental stage and genotypes used can be found in figure legends, methods details, and the key resources table. Female mice between the ages of 6-12 weeks were used for timed pregnancies for embryonic studies. Starting at birth, neonates were weighed weekly. Gait analyses were conducted starting at 2 weeks of age through 6 months of age with age and gender matched cohorts.

Cell lines and culture conditions—Cells were cultured at 37°C in 5% CO_2 in complete media (DMEM or DMEM F12 containing 4.5 g/L D-glucose, [−] Phenol Red, [−] L-Glutamine, [−] HEPES, [−] Sodium Pyruvate, 2 mM L-Glutamine, 1mM Sodium Pyruvate, 1X non-essential amino acids,1% Penicillin Streptomycin solution (Gibco)). MDCK (NBL-2), IMCD3 (CRL-2123), Shh Light II (CVCL_2721) and NIH3T3 (CRL-1658) were obtained from ATCC. *Disp1*$^{-/-}$ knockout (*Disp*^{KO}) MEFs [22,26], and *Disp*^{KO} MEFs stably expressing SHH were described previously [39]. *Myo10*^{WT} and *Myo10*$^{-/-}$ MEFs derived from

male embryos were generated from previous studies[36]. Clonal cell lines stably expressing proteins of interest were developed using the Flp-In system (Thermo Scientific). pCDNA 5 FRT $Disp^{WT}$ or $Disp^{CS}$ (V5/HA tagged) and pOG44 Flp-Recombinase vector were transfected and selected using Hygromycin. IMCD3 cell lines stably expressing $DISP^{WT}$ or $DISP^{CS}$ (V5/HA tagged) were generated using the Flp-In system to create LacZ-FRT single clones then pCDNA 5 FRT $DISP^{WT}$ or $DISP^{CS}$ (V5/HA tagged) were transfected and selected using Hygromycin. Flp-In mIMCD3s were virally infected with Dox-inducible SHH using pLVX-Tet-On 3G system (Takara Bio) treated with a viral MOI of 2. Following blasticidin selection, cells remained in G418 to maintain stable integration. All cell lines were routinely validated by functional assay and western blot as appropriate and tested monthly for mycoplasma contamination by MycoAlert (Lonza). Transfection of plasmid DNA for transient protein expression was performed with Lipofectamine 3000 and P3000 reagent (Thermo Fisher Scientific) per manufacturer's instructions. When required, the final molar amount of DNA used for transfection was kept constant by the addition of control vector DNA.

METHOD DETAILS

Disp mice generation—The *Disp1*^{INDEL} (−11bp) and *Disp1*^{CS} mutant mouse models were created using CRISPR-Cas9 technology and direct zygote injection. sgRNAs were designed to have at least 3 base pairs (bp) of mismatch to any other site in the mouse genome and to bind within 50 bp of the desired modification site. Two chemically modified sgRNAs (Synthego) were tested prior to embryo injection for activity in mouse Neuro-2A cells (ATCC) stably expressing Cas9 and assayed by targeted next generation sequencing (NGS) as described (DOI: 10.1038/s41598-018-19441-8)[86]. Resulting NGS data were analyzed using CRIS.py (DOI: 10.1038/s41598-019-40896-w)[87]. The sgRNA with the highest cleavage activity (SNP5.DISP1.g15) was used for zygote injections. An ssODN donor (10ng/ul, IDT) was co-injected with Cas9 mRNA (10ng/ul, TriLink) and SNP5.DISP1.g15 (5ng/ul) for the creation of the *Disp1*^{CS} mouse model. The ssODN was designed with 60 bp homology arms, the desired ^{278}AAA mutation, and a silent blocking modification to prevent recutting after a successful integration event. The *Disp1*^{INDEL} mouse model resulted as a biproduct from a nonhomologous end joining event after cleavage with SNP5.DISP1.g15. Zygotes were injected and transferred to 0.5 dpc pseudopregnant fosters (7–10 weeks old females mated to vasectomized males) [88]. Editing constructs and relevant primers are in Table S1. After the correctly modified founder animals were confirmed, mice were backcrossed four generations.

Magnetic resonance imaging—Magnetic resonance imaging (MRI) was performed on a Bruker Clinscan 7T MRI system (Bruker Biospin MRI GmbH, Ettlingen, Germany). Prior to scanning, mice were anesthetized in a chamber (3% Isoflurane in oxygen delivered at 1 L/min) and maintained using nose-cone delivery (1-2% Isoflurane in oxygen delivered at 1 L/min). Animals were provided thermal support using a heated bed with warm water circulation and a physiological monitoring system to monitor breath rate. MRI was acquired with a mouse brain volume coil positioned over the mouse head and placed inside a 72 mm transmit/receive coil. After the localizer, a T2-weighted turbo spin echo sequence was performed in the horizontal (TR/TE = 3080/40 ms, matrix size = 256 x 256, field of view

= 36 mm x 36 mm, slice thickness = 0.5 mm, number of slices = 20), coronal (TR/TE = 4760/42 ms, matrix size = 192 x 192, field of view = 15 mm x 15 mm, slice thickness = 0.5 mm, number of slices = 30), and sagittal (TR/TE = 3580/39 ms, matrix size = 128 x 256, field of view = 16 mm x 32 mm, slice thickness = 0.5 mm, number of slices = 24) orientations. Analysis of the MRI images was performed in 3D Slicer (Surgical Planning Laboratory). The coronal images were opened, and a new segmentation was added. Regions of interest were made for the whole brain by painting only the areas of the image that contained the brain. This continued for all slices until the whole brain was painted. The volume of the brain was determined by measuring the volume of the painted region calculated from the voxel dimensions. Similarly, a second segmentation was created for the cerebellum, and its volume was calculated in the same manner.

Computed Tomography—Computed Tomography (CT) was performed on a Siemens Inveon PET/CT system (Siemens, Erlangen) at 45 μm isotropic resolution. Mice were anesthetized and supported as described above. Total scan time was 16 minutes 34 seconds long. Analyses of the CT images were completed using the Inveon Research Workplace software (Siemens). The L1 – L10 measurements were determined based on predefined measurement locations (see Figure S1).

Gait Analysis—A 60 cm long, 5 cm wide runway was lined with Whatman paper. Mice (2 weeks to 6 months) were trained to walk through the runway before conducting the experiment. The paws of the mice were painted with two distinct colors for the forelimbs (blue) and hindlimbs (red). For each mouse, at least 3 runs (n=30-45 steps per animal) were recorded and analyzed. Gait ratio (b/a) for each limb was determined by footprints distance between the left paw to the next step between left (a) and corresponding right paw (b) (DOI: 10.1111/j.1601-183X.2004.00072.x) [89]. See Figure 1I for visualization.

Neural tube Imaging—Wild type C57BL/6J (JAX#000664), Rosa 26 *mT/mG* (JAX # 007676), *Shh-Cre* (JAX # 005622), *Shh::gfp* (JAX # 008466), *Myo10*^{m1J} (JAX # 024583), and *Disp1* mutant embryos in the C57BL/6 background were harvested and processed for immunohistochemistry. E8.5 (8-15 somites) or E9.5 (25-30 somites) stage embryos were used for analyses and embryos of the same somite number were compared. Pregnant dams were harvested, uterine horns removed, and embryos were dissected in 1X PBS, then rinsed three times. Whole embryos were imaged on a Stereo Microscope (Leica). Embryos were fixed for one hour at room temperature in 4% PFA, rinsed three times in 1X PBS, and then moved to 30% sucrose to cryo-protect. The following day, embryos were frozen in O.C.T. Compound (Tissue-Tek) on dry ice. Embryos were sectioned transverse at 10 μm thickness on a Leica Microm CM1950 cryo-stat. Sections were briefly dried, washed in 1X TBST, and then blocked with 2% BSA, 1% goat serum, 0.1% Triton-X-100 in 1X PBS. Antibodies were diluted in blocking buffer and incubated overnight on sections at room temperature in a humidified chamber. The following antibodies and dilutions were used: chicken anti-GFP (1:500, Aves, GFP-1020), mouse anti-PAX6 (1:25, DSHB, PAX6), rabbit anti-OLIG2 (1:300, Millipore, AB9610), rabbit anti-FOXA2 (1:250, abcam, ab108422), rabbit anti-OLIG3 (1:500, Thermo Fisher, JE56-40), rabbit anti-pSMAD 1/5/9 (1:1000, CST, 13820) and rabbit anti-NKX2.2 (1:200, Novus Bio, NBP1-82554). Primary antibody was

removed, sections were washed with 1X TBST three times, then incubated for 3 hours in secondary antibodies (Invitrogen) used at a 1:500 dilution. Sections were washed three times in 1X TBST, then rinsed with tap water, dried, and cover slips were applied with ProLong Diamond mounting media. Sections were imaged on a Leica DMi8 widefield microscope and processed using LAS X. A minimum of five embryos per genotype were analyzed.

For RNAscope, E9.5 embryos were harvested, fixed, embedded, and sectioned as described above. Following mounting, sections were stained with MmGli1-C1 probe (ACDBio #311001) using the RNAscope™ Multiplex Fluorescent Reagent Kit v2 (ACD) following manufacturer's protocol (document 323100-USM). Antigen retrieval was performed for 10 minutes, with 30 minutes of Protease-III treatment. For signal development, Opal-570 was used at 1:1000.

For *in situ* hybridization, E9.5 embryos were harvested and fixed for 4 hours at 4°C in 4% PFA. In situ hybridization experiments were performed as described (DOI: 10.3791/2912)[90] with the following modifications. Frozen embryos were sectioned transverse at 15 μm thickness and mounted on charged glass slides. The sense and antisense digoxigenin-labeled RNA probes were made using a DIG RNA labeling kit following the manufacturer's instructions (Roche). Sense probes were used as negative controls and no positive signal was observed. Three embryos per genotype were analyzed.

Quantification of neural tube sections was performed using Fiji (ImageJ) (DOI: 10.1038/nmeth.2019) [91]. All analyses were performed on cardiac level transverse sections that were identified by positioning of the branchial pouches, aortic sac, and size/morphology of atria/ventricles. The Kaufman Atlas of Mouse Development Plate 19b images g-h show the region of our cardiac level images shown in Figure 2 and analyzed for expression domain quantification [92]. Transverse cardiac level sections adjacent to somite 2 were analyzed by measuring neuron progenitor marker (PAX6, OLIG2, NKX2.2, FOXA2) expression domain area relative to the entire neural tube area. Three to 5 embryos were analyzed per genotype with 5-8 sections analyzed per embryo. Expression domain areas were calculated by measuring the area of the indicated expression domain and normalizing it to the total area of the neural tube in each section analyzed.

Expression domain intensity line plot data were generated as previously reported (DOI: 10.1371/journal.pbio.1002119)[93]. Briefly, a 20 pixel-wide line was traced through the center mass of neuroepithelial cells on each side of the neural tube. Lines were drawn from the basal surface of the floor plate midline to the basal surface of the roof plate midline. A total of 4-8 sections per embryo from 3 embryos per genotype were analyzed. Individual line plots were normalized with minimum value set to 0 and maximum value set to 100, except for *Gli1* in situ hybridization plots which were not transformed and based on detected fluorescence. Data are represented as average intensity across all lines ± SEM. Relative and absolute dorsal/ventral position of progenitor markers were measured like the line plot data, with values based upon distance from the floor plate midline to the roof plate midline through the center mass of neuroepithelial cells. Relative position values were determined as a ratio of total FP to RP trace length for each section analyzed. Expression domain dorsal start position and ventral endpoints were recorded for each marker and compared across

genotypes. Vertical D/V length was measured from the FP midline to RP in a straight line. Five to 8 sections per embryo from 3 embryos per genotype were analyzed.

Cytoneme preservation and imaging in mouse embryos—Embryos were prepped for cytoneme analysis as described (DOI: 10.3791/64100) [57]. Embryos were dissected in complete growth media and then rinsed in Hanks' Balanced Salt Solution (HBSS). Embryos were fixed for 45 minutes in HBSS plus 4% paraformaldehyde with very gentle rocking. After fixation, embryos were washed three times in PBS with Ca^{2+} and Mg^{2+} and 0.1% Triton for 30 minutes each wash. Embryos were incubated twice for one hour in block (PBS with Ca^{2+} and Mg^{2+}, 0.1% Triton, and 5% goat serum) with gentle agitation. Embryos were then incubated in primary antibody solution (antibodies were diluted in PBS with Ca^{2+} and Mg^{2+}, 0.1% Tween-20, and 5% goat serum) for 72 hours at 4°C with gentle rocking. The following antibodies were used: chicken anti-GFP (1:250, Aves, GFP-1020), mouse anti-SHH (1:100, DSHB, 5E1 supernatant), rabbit anti-OLIG2 (1:300, Millipore, AB9610) and rabbit anti-ARL13B (1:500, Proteintech, 17711-1-AP). Following primary incubation, embryos were washed 5 times for an hour in block under gentle agitation. Embryos were incubated in $F(ab')_2$ fragment secondary antibody solution (1:1000 antibody diluted in block) for 72 hours with gentle rotation at 4°C in the dark. If no actin staining was required, embryos were incubated with DAPI for 1 hour and then washed in block 3 times for 10 minutes each. A final series of three 20-minute washes in PBS with Ca^{2+} and Mg^{2+}, 0.1% Tween-20 was performed, and embryos were held in solution prior to embedding.

Embryos were mounted in 4% low melting point agarose dissolved in HBSS or PBS with Ca^{2+} and Mg^{2+}. Embedded embryos were sectioned with a vibratome at 100 or 150 μm. For F-actin staining, sections were incubated with ActinRed (ThermoFisher) and DAPI for 40 minutes. Sections were then washed once in block then two times in PBS with Ca^{2+} and Mg^{2+}, 0.1% Tween-20 for 20 minutes each wash. Sections were mounted on slides using Prolong Diamond. Tissue sections were imaged with a TCS SP8 STED 3X confocal microscope (Leica), followed by LIGHTNING deconvolution or a Stellaris tauSTED (Leica) with active tau-gating in photon-counting mode. A minimum of 3 embryos per genotype were analyzed with all comparison between genotypes done with equal numbers of somite matched embryos. To mitigate interference from low-level nonspecific GFP signal, all SHH *in vivo* quantifications were calculated using anti-SHH signal.

Cytoneme preservation and analysis in cell culture—Cell fixation and staining were performed using MEM-fixation protocols (DOI: 10.21769/BioProtoc.2898)[94]. Following transfection and replating onto coverslips, cells were fixed in a 4% formaldehyde, 0.5% glutaraldehyde and 0.1 M Phosphate buffer (pH 7.4) solution for 7 minutes. From this point onwards, all solutions were gently pipetted to minimize agitation to the plates during washes. After fixation, cells were washed thrice in PBS for 5 minutes each wash. Cells were permeabilized in buffer consisting of 5% normal goat serum and 0.1% Triton X-100 in a 1 mg/ml sodium borohydride solution that was dissolved in distilled water for 45 minutes. Please see the “Immunofluorescence and Imaging Staining Protocols” section for details on antibody incubation.

We defined cytonemes for quantification as cellular projections approximately <200 nm in diameter with a minimum length of 10 μm (DOI: 10.7554/eLife.61432) [36]. Any cellular protrusions that maintained continuous contact with the coverslip along their entire lengths were excluded from analysis [94]. Cytoneme occurrence rate counts were performed with a minimum of 100 cells per condition across 3 coverslips with a minimum of two biological replicates. Cytoneme to cell body fluorescent intensity ratios were calculated by measuring mean fluorescent intensity of the individual cytonemes over the mean fluorescent intensity of its originating cell body with a total of n=44-80 cytonemes analyzed per condition from 3 biological replicates. Linear regression analysis of DISP variants to SHH-GFP in cytonemes was analyzed by measuring relative fluorescent intensity ratios of each protein within the same cytoneme, n=44 or 46 cytonemes analyzed from 2 biological replicates.

Cytoneme-based SHH signal activation was measured using Ca^{2+} flux rates in SHH receiving cells as described [36]. Briefly, a total of 2 μg plasmid DNA was transfected into cells of individual wells of a 6 well plate. pCMV-R-GECO1 for NIH3T3 'receiving' sensor cells, and the pCDNA3-mSHH-FL-EGFP for the DISP variant MEF 'producing' cells. Twenty-four hours after transfection, cells were trypsinized and replated into eight well, polystyrene chambers on a 1.5 borosilicate cover glass, 0.7 cm^2/well (Nunc Lab-Tek II). Cells were seeded into chambered wells at ~40% cell density (20% R-GECO, 20% SHH-GFP) and allowed to recover for a minimum of 4 hours before imaging. Cells were gently washed in PBS, and media was replaced with fresh media to remove secreted SHH prior to imaging to ensure signal originated from cytoneme-delivered ligand. Live imaging was performed at 37°C, 5% CO_2 with resonant scanning for 15 min per area over the entire cytoneme depth (~4-6 μm) with Z-steps of ~0.6-1.0 μm. Maximum intensity projections were generated for subsequent analysis of the time-lapses. R-GECO fluorescent intensity histograms of individual cells were normalized for each cell with minimum fluorescence equal to 0 and maximum to 100. Ca^{2+} flux occurrence was quantified as a relative peak in R-GECO fluorescence within a ~20 s window with a minimum peak fluorescence of 50. Only R-GECO cells in contact with cytonemes from SHH-GFP producing cells were quantified for analysis, with any R-GECO cell that did not exhibit a single flux during the scan time were excluded from analysis. A total of n=31-41 cells were analyzed per condition from 3 biological replicates.

Analysis of SHH puncta along cytonemes from the notochord and neural tube lumen.—A workflow pipeline was developed to quantify the amount of SHH traveling from the notochord to surrounding cells and tissue along cytonemes. The unprocessed anti-SHH channel from ~50-90 images taken at 0.33 μm z-step intervals was extracted from the scan series using Fiji (Image J)[91] and subjected to Fast Fourier Transform (FFT) Bandpass filtering with background subtraction. The remaining channel stains (DAPI, F-actin, anti-GFP) were merged and summed to act as a cell outline mask. The cell outline mask series were then run through Ilastik (DOI: 10.1038/s41592-019-0582-9)[95] training to generate a segmentation mask series defining cell bodies and cytonemes. Segmentation masks and the filtered SHH series were then reconstituted in Fiji[91] with the image calculator function. Quantification of SHH puncta along cytonemes from the notochord was determined by thresholding (thresholding was carried out using max entropy analysis, with a range of

10-100) followed by particle analysis set to 10-60 pixels to exclude excessively small or large puncta. Nine to 15 tissue sections, representing 440-797 images, were analyzed per genotype.

Quantification of lumen SHH puncta in E8.5 embryos was performed by thresholding and counting puncta within the first 10 μm (~30 z-steps) of the tissue section with Fiji[91]. Puncta in the same position across sequential z-steps were counted only once. A total of 18-20 sections from 6-8 embryos per genotype were analyzed. To quantify SHH neural tube lumen (NTL) signal intensity, a region of interest (ROI) along the NTL was drawn with a second ROI within NT cell body to be used as a background correction. Mean signal intensity per section was determined by mean NTL signal minus mean NT signal. All *in vivo* quantification was performed using anti-SHH signal.

RNA sequencing—*Disp1*$^{CS/+}$ females were crossed with *Disp1*$^{INDEL/+}$ males to generate litters of E9.5 control (wild type) and *Disp1*$^{CS/INDEL}$ embryos. Similarly, *Myo10*$^{m1J/+}$ females were crossed with *Myo10*$^{m1J/+}$ males to generate litters of E8.5 control (*Myo10*$^{+/+}$) and *Myo10*$^{m1J/m1J}$ embryos. Multiple litters were harvested and five pairs of somite matched littermates (5 control, 5 mutant) were used per genotype to maximize genetic variability. Pregnant dams were harvested, embryos were dissected, and each embryo was placed in a 1.5 mL Eppendorf tube and flash frozen in liquid nitrogen, then stored at −80C while genotyping was performed. Once 5 pairs of embryos were generated, all samples were purified at the same time. Each whole embryo was homogenized, and RNA was extracted by using RNeasy Micro Kit (Qiagen) using the manufacturer's protocol. RNA sequencing libraries for each sample were prepared with 1 mg total RNA by using the TruSeq RNA Sample Prep v2 Kit (Illumina) per the manufacturer's instructions, and sequencing was completed on the Illumina NovaSeq 6000. The 100-bp paired-end reads were trimmed, filtered against quality (Phred-like Q20 or greater) and length (50-bp or longer), and aligned to a mouse reference sequence GRCm39 (UCSC mm39) by using CLC Genomics Workbench v20.0.4 (Qiagen). The TPM (transcript per million) counts were generated from the CLC RNA-Seq Analysis tool. The differential gene expression analysis was performed by using the non-parametric ANOVA using the Kruskal-Wallis and Dunn's tests on log-transformed TPM between four biological replicates from each of two experimental groups, implemented in Partek Genomics Suite v7.0 software (Partek Inc.). The gene sets enrichment and pathway analysis were performed using GSEA (DOI: 10.1073/pnas.0506580102) [96]. Data sets have been deposited on Gene Expression Omnibus and are publicly available under Accession number (GSE242161).

Immunofluorescence and image acquisition for cell culture—Cells were grown on coverslips and then rinsed 3 times in PBS and fixed in 4% paraformaldehyde, followed by three 5-minute washes in PBS + 0.1% Triton. Cells were incubated in block (PBS, 0.1% Tween-20, and 5% goat serum) for an hour, and then incubated overnight in primary antibody. The following antibodies were used: rabbit anti-SHH (1:100, Santa Cruz, H-160), rat anti-HA (1:250, Roche, 3F10), mouse anti-V5 (1:300, Life Technologies, SV5-Pk1), mouse anti-Rab5A (1:800, CST, 46449), rabbit anti-Rab7 (1:200, CST, 9367), rabbit anti-Rab11 (1:200, CST, 5589), rabbit anti-Rab4 (1:100, Life Technologies, PA3-912) rabbit

anti-Caveolin-1 (1:800, CST, 3267), mouse anti-Clathrin adaptor protein 2 alpha subunit (AP2α) (1:100, Thermo Scientific, AC1-M11), rabbit anti-Clathrin heavy chain (1:100, CST, 4796). The following day, coverslips were washed 3 times in block for 10 minutes and secondary antibodies (Jackson ImmunoResearch and Invitrogen) were used at a 1:1000 dilution, with the addition of DAPI and Actin-Red (Invitrogen) incubated for 1 hour. Coverslips were washed and mounted using Prolong Glass anti-fade mount (Invitrogen). Microscopy images were taken with a TCS SP8 STED 3X confocal microscope (Leica) or A1R confocal (Nikon) for fixed and live cell imaging.

Image processing and analysis—Following image acquisition, images were processed using LAS X (Leica), ImageJ[91], and Photoshop 2022 (Adobe), and figures were made using Illustrator 2022 (Adobe). Neural tube cytoneme imaging acquired on the TCS SP8 STED 3X confocal microscope underwent deconvolution using LIGHTNING software (Leica). Videos were processed with ImageJ[91], LAS X, Amira (ThermoFisher) and Premiere Pro (Adobe). EM image data were analyzed and processed using Amira (ThermoFisher), Ilastik [95], and Collaborative Annotation Toolkit for Massive Amounts of Image Data (CATMAID) (DOI: 10.1093/bioinformatics/btp266)[72,97]. Images are presented as maximum intensity projections (MIP) of the z-stack acquisition spanning the cell or area of interest, unless stated otherwise. Images shown represent a standard cell or tissue section from a minimum of three biological replicates across multiple experiments unless stated otherwise.

Plasmids—The following plasmids were used in this study: pCDNA (control vector) (Clontech V79020), pCMV3-hBMP2-GFPSpark (Sino Biological HG10426-ACG), pCMV3-hBMP4-OFPSpark (Sino Biological HG10609-ACR), pCMV3-hBMP7-GFPSpark (Sino Biological HG10083-ACG), pCMV3-hWNT1-GFPSpark (Sino Biological HG10721-ACG), pCDNA3-EGFP (Addgene Plasmid #13031), pCMV-mCherry-Membrane [98](Addgene Plasmid #55779), pCMV-R-GECO1 [99](Addgene Plasmid #32444), pCMV-mCherry2 (Addgene Plasmid #54517), pCDNA3.1-mSHH-FL [39], pCDNA3.1-mSHH-FL-EGFP [36], pCDNA3.1-mSHH-FL-mCherry2 [36], pCDNA3.1-V5-DISP^{CS}-HA [39](Addgene plasmid #126410), pCDNA3.1-V5-DISP^{CS}-HA [39], pCDNA3.1-V5-DISP$^{\Delta C}$-HA, pCDNA3.1-V5-DISP^{4xAA}-HA, pCDNA3.1-V5-DISP^{WT}-Dronpa3-HA, pCDNA3.1-V5-DISP^{CS}-Dronpa3-HA, pCDNA3.1-DISP$^{\Delta C}$-Dronpa3-HA. Dronpa3 constructs were derived from Dronpa3-N1 (Addgene Plasmid #54682) and inserted between DISP residues A695 and V696. Dronpa3 constructs were amplified with BsrG1 (NEB) restriction sites before insertion into Dispatched IC3 using Phusion PCR (NEB). AP2/Clathrin binding mutants DISP$^{\Delta C}$ and DISP^{4xAA} were created using Quik change mutagenesis (Quik Change II XL site-directed mutagenesis kit, Agilent, 200522).

Dronpa3 BsrG1 primers:

Forward:5’ tatagatccACCGGTCtgtacaATGGTGAGTGTGATT 3’

Reverse: 5’ tataAGTCGCGGCCGCCTAtgtacaCTTGGCCTGCCT 3’

Quick change primers:

C-terminal Deletion 5’gagccaggctcagccCTCGAGtacccctac 3’

DISP1 L1249/1250A primers:

Forward: 5’ ccaggctcagccgcggcgcagtcctgtctg 3’

Reverse: 5’ cagacaggactgcgccgcggctgagcctgg 3’

DISP1 L1324/1325A primers:

Forward: 5’ caagccgccgagggcgctgcgcaccctgcccag 3’

Reverse: 5’ ctgggcagggtgcgcagcgccctcggcggcttg 3’

DISP1 L1441/1442A primers:

Forward: 5’ gtggagccaagcgcggcgcagaccgatgaa 3’

Reverse: 5’ ttcatcggtctgcgccgcgcttggctccac 3’

DISP1 L1516/1517A primers:

Forward: 5’ actcagacctgtctggcgagagtgcggcaataaaaacactactcgagtacc 3’

Reverse: 5’ ggtactcgagtagtgtttttattgccgcactctcgccagacaggtctgagt 3’

Protein stability cycloheximide assay—*Disp*^{KO} Flp-In MEFs stably expressing V5-DISP^{WT}-HA or V5-DISP^{CS}-HA were transiently transfected with pCDNA3.1-mSHH-FL or empty vector control. After transfection, cells were replated into 60 mm^2 tissue culture dishes and incubated overnight. Cycloheximide (20μg/mL, dissolved in DMSO) was added to all plates. Plates were harvested at 0, 2, 4, 6, 8, 12 hours lysing with 1x RIPA buffer (Thermo Scientific). Cell lysates were normalized for protein content and were probed for DISP (rat anti-HA, 1:2000, Roche, 11867423001) and loading control mouse anti-α-Tubulin (1:10000, CST, DM1A) by western blot. The ratio of the protein remaining over time was calculated using densitometry (ImageJ)[91] of time point divided by densitometry of the 0-time point.

Immunoblotting and immunoprecipitation—For western blotting, SDS-PAGE samples were run on 4-15% Tris-glycine SDS-PAGE gels (Bio-Rad) and transferred onto Immobilon-P PVDF (Millipore) using Tris/Glycine/SDS Buffer (Bio-Rad) at 100V for one hour. Membranes were blocked with 5% milk in Tris-buffered saline with 0.1% Tween-20 (TBST) or 5% BSA inTBST for 1 hour at room temperature. Antibody dilutions were as follows anti-HA (1:3000; Roche 3F10), anti-V5 (1:2000; Life Technologies SV5-Pk1), anti-SHH (1:2000; CST C9C5), Rabbit anti-Kinesin (anti-Kif5B, 1:5000; Abcam ab167429), and/or Tubulin (1:10,000; CST DM1A), Alpha Adaptin (1:1000, Thermo Scientific AC1-M11), Beta Adaptin (1:1000, Bethyl Biosciences A304-718A). Corresponding HRP-conjugated secondary antibodies (Jackson Immuno) were incubated for 1 hr at RT at a 1:5000 concentration. Infrared antibodies (Li-Cor) were used at a 1:10000 concentration with HRP-conjugated antibodies when duplexing. Blots were developed by using an Odyssey Fc (Li-Cor) with ECL Prime (GE).

Biotinylation assays and subsequent densitometry were performed as described in Marada et al. 2015 (DOI: 10.1371/journal.pgen.1005473) [100]. Briefly, live cells were washed three times with cold PBS (pH 7.4) and then incubated with gentle shaking for 30 minutes at 4°C in PBS containing 0.5 mg/ml EZ-Link Sulfo-NHS-Biotin (Thermo Scientific). Biotinylation was quenched by washing cells twice with cold PBS containing 50 mM Tris. Cells were harvested and lysed in RIPA buffer. Lysates were incubated with 50 µl of Streptavidin agarose beads (Thermo Scientific) for 1 hour at 4°C. Beads were then washed three times with RIPA buffer and bead-bound proteins were extracted in boiling sample buffer containing 2 mM free biotin. Proteins from the supernatant and eluted from Streptavidin beads were analyzed by SDS-PAGE and western blot. Densitometry analysis was performed using Fiji and the ratio of signal densities for Streptavidin-bound cell surface vs. lysate DISP was determined.

For immunoprecipitation, mouse embryonic fibroblasts stably expressing full length SHH were transiently transfected to express wild type, CS mutant, or ΔC DISP proteins. Cells were then cultured, and the plasma membrane fractions were isolated in modified HK Buffer ((20 mM HEPES, 10 mM KCl; pH 7.9)+ 2.5% Glycerol+50 mM NaCl) as described [101]. Protein content was normalized, membrane fractions were pre-cleared with protein A/G Plus agarose (Santa Cruz SC-2003), samples were immunoprecipitated for HA using EZview Red Anti-HA Affinity Gel (E6779-1ML, Millipore Sigma) for 1.5 hours at 4°C. Beads were then subjected to 3 x 5 min washes at room temperature in lysis buffer plus 150 mM NaCl and eluted in 5X SDS Buffer at room temperature. Samples were analyzed by SDS-PAGE and western blot for AP2 and DISP-HA (α-Adaptin (1:1000, Thermo Scientific AC1-M11), β-Adaptin (1:1000, Bethyl Biosciences A304-718A), HA (1:3000, Roche, 3F10)).

Spheroid generation and analysis—IMCD3 cells stably expressing wild type or CS mutant V5-DISP-HA proteins and doxycycline-inducible SHH were used to generate spheroids as described (DOI: 10.1038/nprot.2014.181) [51]. Twenty-four hours prior to spheroid fixation, media was replaced with control or 100ng/mL doxycycline media to induce SHH expression. The following day, spheroids were fixed and stained following established protocols [51]. Spheroids were stained for rabbit anti-SHH (1:100, Santa Cruz, H-160), rat anti-HA (1:250, Roche, 3F10), mouse anti-V5 (1:300, Life Technologies, SV5-Pk1). F-actin and DAPI staining were performed during secondary antibody staining (1:1000). Following staining, IMCD3 spheroids were mounted in Fluoromount-G (Thermo Fisher) and imaged on a Nikon A1R scanning confocal microscope.

Scans were performed at 0.4 µm intervals across the entire spheroid body. Only spheroids that contained a well-defined lumen and cells that were in a monolayer were used for analysis. Analysis was performed on individual cells at center of the cell (section where DAPI takes up the maximum volume of the cell). Individual cell apical and basal surfaces were defined by maximum F-actin fluorescence. DISP localization distribution curves of HA were calculated as an intensity line plot taken along the basal to apical cell membrane. Data were normalized for mean intensity across the membrane equal to 1 with n= 21-29 cells analyzed per condition, taken from 3 biological replicates across multiple experiments. For apical over basal fluorescent intensity ratios, mean intensity values along the apical and basal surfaces of cells (defined by peak F-actin intensity) for individual antibody stains

were measured and compared per cell. Values < 1 indicate predominantly basal protein accumulation and > 1 indicate apical accumulation (lumen surface) with n= 40-47 cells per condition taken from 3 biological replicates across multiple experiments.

Colocalization analysis—Colocalization between DISP-HA and the individual endosomal markers was analyzed within endosomal areas of individual cells. Pearson's correlation coefficient values represent the portion of DISP within the analyzed endosomal compartment and is not representative of the entire cell volume. To perform analysis, scanned cell volumes were generated as maximum intensity projections (MIPs). Ilastik[95] was used on the output MIPs of the endosomal stain to generate segmentation masks highlighting the endosomal marker. MIPs and masks were then run through a secondary pipeline in CellProfiler (DOI: 10.1371/journal.pbio.2005970) [102] to segment and count cells while measuring Pearson's correlation coefficient. The input images include 1) F-actin or SHH-mCherry (for transiently transfected MEFs) to outline and segment individual cells in the scan area, 2) DAPI as a reference node for F-actin segmentation and to number cells per scan area, 3) HA to measure DISP, 4) The endosomal marker to measure the endosomal marker of interest, and 5) Segmentation mask to refine colocalization analysis area to the endosomal marker. Markers were sorted and input into the pipeline, following appropriate thresholding of HA and the endosomal marker, correlation coefficients were calculated per cell within the endosomal compartment. Any F-actin-marked cell areas in the output data below ~15 percentile were excluded from data sets to avoid dying or fragmented cell portions. In these experiments, n= 60-126 control transfected cells and n= 23-39 transfected SHH cells were analyzed from 3 biological replicates across multiple experiments.

DISP membrane internalization—MDCK cells expressing $DISP^{WT}$-Dronpa3, $DISP^{CS}$-Dronpa3, or $DISP^{\Delta C}$-Dronpa3 with either mCherry-Membrane or SHH-mCherry were plated onto Lab-Tek II Chamber slides and allowed to grow until they formed a monolayer. Cell media was aspirated and replaced with serum free media containing 10 mM HEPES. Cells were imaged on a TCS SP8 STED 3X confocal microscope (Leica) equipped with an enclosure box heated to 37°C, 5% CO2 for 80 minutes at 2.5-minute increments with z-series covering the entire cell volume of the monolayer. DISP-Dronpa3 constructs were imaged for 30 minutes to monitor effects of any photobleaching or phototoxicity (none were detected). Endocytosis was blocked with the addition of 25 μM Pitstop 2 (ab120687, abcam, dissolved in DMSO) to the media, resulting in the accumulation of DISP-Dronpa3 to the cell surface over a 30-minute period. Following this, Pitstop 2 treatment serum free media was replaced with media containing 10% FBS, then imaging continued for 50 minutes every 2.5 minutes to measure recovery.

Membrane accumulation and subsequent internalization rates of DISP-Dronpa3 constructs were measured by ROI's marked along cell-cell interfaces of adjacent cell membranes during the time course. Fluorescent intensity of Dronpa3 along the membrane was recorded using LAS X software. Data were normalized per individual ROI with fluorescent intensity at time point zero after Pitstop 2 addition equal to 1. Following Pitstop 2 washout, the fluorescent intensity at time point zero was also normalized to 1. A total of n=31-57

cell ROIs per condition were analyzed taken from 3 biological replicates over multiple experiments.

Luciferase reporter assays—*Disp*^{KO} MEFs stably expressing *MSCV-Hygro* or *MSCV Hygro-Shh* were seeded at a density of 5×10^5 cells per well in a 6-well plate. The following day, *pcDNA3-V5-WT Disp-HA* (3 μg), or *pcDNA3-V5-CS Disp-HA* (3 μg) were transfected into *Disp*^{KO} cells expressing vector or *Shh*. Meanwhile, polystyrene cloning cylinders (9.5 mm inner diameter x 6.2 mm height, Scienceware, Bel-Art) were sterilized in 70% ethanol, washed in sterile PBS, dried, and placed in the center of each well of a 12-well plate, creating a barrier between the inner ring of the well and the outer ring of the well, as previously described [39]. Shh Light II reporter cells [103,104] were seeded at 1×10^5 cells per well around the outer ring of the cylinder. *Disp*^{KO} stable cells transfected with the indicated *Disp* expression vectors were seeded at a density of 5×10^4 cells per well in the inner ring of the cylinder. Cells were allowed to recover overnight. The following day, media was removed from the cells and the cylinders were removed, creating a cell-free barrier between the Shh Light II and *Disp*^{KO} cells. Cells were washed 3 times with PBS and then DMEM Serum-Free Complete media. DMEM Serum-Free Complete media was added back to each well and allowed to incubate for 2 hours. Media was replaced every 2 hours for a total of 6 hours. After 6 hours, 1 mL of DMEM Serum Free Complete Media was added to each well and the cells were allowed to incubate for ~36 hr. Reporter assays were carried out according to Dual Luciferase Reporter Assay Kit instructions (Promega). Experiments were repeated three times in triplicate and all data pooled.

Scanning electron microscopy and quantification—E9.5 embryos (n=8) were fixed in 2.5% glutaraldehyde, 2% paraformaldehyde in 0.1 M cacodylate buffer containing 2 mM $MgCl_2$. Following fixation, samples were decapitated, then a needle was inserted into the anterior neural tube and used to bisect the embryo sagittally to expose the interior of the neural tube lumen, floor plate, and notochord. Dissected samples were buffer washed, post-fixed in 0.1% aqueous osmium tetroxide for 1 hour, washed with ddH_2O, dehydrated with an ascending ethanol series, and critical point dried in liquid CO_2 using an Autosamdri 931 (Tousimis). Dried samples were sputter-coated under planetary rotation with 15 nm iridium and imaged in a ThermoFisher Scientific Teneo scanning electron microscope at 2 kV using the Everhart-Thornley and T1 detectors. Micrograph analysis of neural tube lumen cellular extensions to primary cilia contact were performed by isolating extension and primary cilia with Ilastik [95] to generate segmentation masks. Secondary manual segmentation was utilized to validate cilia. Segmentation masks were then input into ImageJ[91] to assign object counts and measure overlay (contact) by Manders coefficient analysis. Four to 10 micrographs per genotype were analyzed for a total of 1784 primary cilia and 39070 extensions (n=344 *Disp1*$^{+/+}$, n=684 *Disp1*$^{INDEL/+}$, and n=756 *Disp1*$^{INDEL/INDEL}$ primary cilia). Thresholds for extensions count inclusion were adjusted to include any objects larger than the cilia for each micrograph. We validated the accuracy of our automated pipeline by manually counting cilia contacts on one embryo (a total of 389 primary cilia from 5 micrographs). Automated analysis of the embryo determined 53.89% of primary cilia were in contact with cellular extensions with a SD of 15.44, while manual analysis gave 52.18% contact with SD of 10.16, indicating our pipeline was accurate.

Serial Block Face Scanning Electron Microscopy—E9.5 *Disp1*$^{+/+}$, *Disp1*$^{CS/+}$, *Disp1*$^{INDEL/+}$, *Disp1*$^{CS/INDEL}$, *Disp1*$^{INDEL/INDEL}$, *Myo10*$^{+/m1J}$, *and Myo10*$^{m1J/m1J}$ embryos were fixed in 2.5% glutaraldehyde, 2% paraformaldehyde in 0.1M cacodylate buffer. Following fixation, samples were post-fixed in 2% osmium tetroxide in cacodylate buffer for 90 minutes at room temperature, and then transferred directly to 2.5% potassium ferrocyanide in cacodylate buffer. Samples were thoroughly rinsed with ddH2O and incubated at 40°C for 45 minutes in 1% thiocarbohydrazide and again thoroughly washed prior to being incubated in 2% aqueous osmium tetroxide at room temperature for 90 minutes. Samples were rinsed with ddH2O and incubated in 1% aqueous uranyl acetate overnight at 4°C then warmed to 50°C for 30 minutes, held at room temperature for 1 hour and returned to 50°C for 30 minutes. Following thorough rinsing with ddH2O, samples were dehydrated in an ascending series of ethanols, transitioned in propylene oxide and infiltrated with EMBed-812 epoxy resin. Samples in 100% EMBed-812 were polymerized at 60°C for 2 days. Selected samples were trimmed, mounted, coated with iridium and mounted for imaging in a Thermo Fisher Scientific Teneo VolumeScope SEM. Imaging conditions, including water vapor pressures for charge mitigation, were adjusted on a per sample basis to ensure consistent imaging and cutting. A minimum of 2 embryos per genotype, with 2 individual scan series per embryo were performed. Individual scan series consisted of roughly 500-1000 serial sections spanning a tissue depth of 50-100 μm with a X, Y resolution of 20-40x20-40 nm/pixel with serial sections taken at 60-100 nm intervals. Segment alignment and volume rendered individual cells were generated with Amira (ThermoFisher). Data sets were uploaded to CATMAID [72,97] for quantification of cellular extensions length and frequency. Membrane extensions were segmented and individually mapped through serial sections across the scan area until their end point or cell-cell membrane density exceeded resolution preventing further mapping of extensions. Quantification of the extensions/nuclei values were generated from 10 serial sections at time (~1 μm depth) to confirm membrane blebs were continuous extensions. 5-10 one μm thick section series were analyzed per embryo.

QUANTIFICATION AND STATISTICAL ANALYSIS

The number and developmental stage of mice used in each experiment is given within figures or figure legends. Additional numbers (n) used in analyses are included for individual experiments in the method details. Experiments were not performed in a blinded manner with the exception of analyses of ~E8.5 embryos in MYO10 experiments shown in Figure 7. All statistical analyses were performed using GraphPad Prism. One-way analysis of variance was performed for multiple comparisons, with Tukey's multiple comparison as a posttest. Significant differences between two conditions were determined by two-tailed Student's t tests. Colocalization quantification was performed with CellProfiler[102] or ImageJ (Fiji)[91] with analysis performed by Pearson correlation coefficient or Mander's coefficient where appropriate. All quantified data are presented as mean ± SD unless stated otherwise, with $p<0.05$ considered statistically significant. Significance depicted as *$p<0.05$, **$p<0.01$, ***$p<0.001$, ****$p<0.0001$, ns = not significant.

Supplementary Material

Refer to Web version on PubMed Central for supplementary material.

Acknowledgements

Timothy Sanders and Khaled Khairy consulted on image acquisition and analysis. Mark Hatley provided comments on the manuscript. RNAseq was performed at the Hartwell Center of SJCRH. SBF-SEM data transfer to CATMAID was performed by Center for Bioimage Informatics (CBI) of SJCRH. The St. Jude Transgenic Core (TCU) generated the *Disp1* mutant mouse lines. P. Beachy and A. Salic provided $Disp^{KO}$ MEFs and the Developmental Studies Hybridoma Bank provided antibodies.

Funding

Research was supported by NIH R35GM122546 (SKO), F31HD110256 (CAD), NCI P30CA021765 (SJCRH Cancer Center Support Grant), and ALSAC of St. Jude Children's Research Hospital. The content is solely the responsibility of the authors and does not necessarily reflect the views of the funding agencies.

References

1. Sagner A, and Briscoe J (2017). Morphogen interpretation: concentration, time, competence, and signaling dynamics. Wiley Interdiscip Rev Dev Biol 6, 271. 10.1002/WDEV.271.
2. Stathopoulos A, and Iber D (2013). Studies of morphogens: keep calm and carry on. Development 140, 4119. 10.1242/DEV.095141. [PubMed: 24086076]
3. Barakat MT, Humke EW, and Scott MP (2010). Learning from Jekyll to control Hyde: Hedgehog signaling in development and cancer. Trends Mol Med 16, 337–348. 10.1016/j.molmed.2010.05.003. [PubMed: 20696410]
4. Müller P, Rogers KW, Yu SR, Brand M, and Schier AF (2013). Morphogen transport. Development 140, 1621–1638. 10.1242/dev.083519. [PubMed: 23533171]
5. Zhang C, and Scholpp S (2019). Cytonemes in development. Curr Opin Genet Dev 57, 25–30. 10.1016/J.GDE.2019.06.005. [PubMed: 31404787]
6. Ramírez-Weber FA, and Kornberg TB (1999). Cytonemes: cellular processes that project to the principal signaling center in Drosophila imaginal discs. Cell 97, 599–607. [PubMed: 10367889]
7. Daly CA, Hall ET, and Ogden SK (2022). Regulatory mechanisms of cytoneme-based morphogen transport. Cellular and Molecular Life Sciences 79, 3. 10.1007/S00018-022-04148-X.
8. Bischoff M, Gradilla A-C, Seijo I, Andrés G, Rodríguez-Navas C, González-Méndez L, and Guerrero I (2013). Cytonemes are required for the establishment of a normal Hedgehog morphogen gradient in Drosophila epithelia. Nat Cell Biol 15, 1269–1281. 10.1038/ncb2856. [PubMed: 24121526]
9. Rojas-Ríos P, Guerrero I, and González-Reyes A (2012). Cytoneme-Mediated Delivery of Hedgehog Regulates the Expression of Bone Morphogenetic Proteins to Maintain Germline Stem Cells in Drosophila. PLoS Biol 10, e1001298. 10.1371/JOURNAL.PBIO.1001298. [PubMed: 22509132]
10. Roy S, Hsiung F, and Kornberg TB (2011). Specificity of Drosophila cytonemes for distinct signaling pathways. Science (1979) 332, 354–358. 10.1126/SCIENCE.1198949/SUPPL_FILE/ROY.SOM.REV1.PDF.
11. Sanders TA, Llagostera E, and Barna M (2013). Specialized filopodia direct long-range transport of SHH during vertebrate tissue patterning. Nature 497, 628–632. 10.1038/nature12157. [PubMed: 23624372]
12. Zhang Z, Denans N, Liu Y, Zhulyn O, Rosenblatt HD, Wernig M, and Barna M (2021). Optogenetic manipulation of cellular communication using engineered myosin motors. Nature Cell Biology 2021 23:2 23, 198–208. 10.1038/s41556-020-00625-2. [PubMed: 33526902]
13. Stanganello E, Hagemann AIH, Mattes B, Sinner C, Meyen D, Weber S, Schug A, Raz E, and Scholpp S (2015). Filopodia-based Wnt transport during vertebrate tissue patterning. Nat Commun 6, 5846. 10.1038/ncomms6846. [PubMed: 25556612]

14. Jiang J, and Hui C-C (2008). Hedgehog signaling in development and cancer. Dev Cell 15, 801–812. 10.1016/j.devcel.2008.11.010. [PubMed: 19081070]
15. Briscoe J, and Thérond PP (2013). The mechanisms of Hedgehog signalling and its roles in development and disease. Nat Rev Mol Cell Biol 14, 416–429. 10.1038/nrm3598. [PubMed: 23719536]
16. Pepinsky RB, Zeng C, Went D, Rayhorn P, Baker DP, Williams KP, Bixler SA, Ambrose CM, Garber EA, Miatkowski K, et al. (1998). Identification of a palmitic acid-modified form of human Sonic hedgehog. Journal of Biological Chemistry 273, 14037–14045. 10.1074/jbc.273.22.14037. [PubMed: 9593755]
17. Porter JA, Young KE, and Beachy PA (1996). Cholesterol modification of hedgehog signaling proteins in animal development. Science 274, 255–259. [PubMed: 8824192]
18. Qi X, Schmiege P, Coutavas E, Wang J, and Li X (2018). Structures of human Patched and its complex with native palmitoylated sonic hedgehog. Nature 560, 128–132. 10.1038/s41586-018-0308-7. [PubMed: 29995851]
19. Li Y, Zhang H, Litingtung Y, and Chiang C (2006). Cholesterol modification restricts the spread of Shh gradient in the limb bud. Proc Natl Acad Sci U S A 103, 6548–6553. 10.1073/pnas.0600124103. [PubMed: 16611729]
20. Burke R, Nellen D, Bellotto M, Hafen E, Senti KA, Dickson BJ, and Basler K (1999). Dispatched, a novel sterol-sensing domain protein dedicated to the release of cholesterol-modified hedgehog from signaling cells. Cell 99, 803–815. [PubMed: 10619433]
21. Caspary T, García-García MJ, Huangfu D, Eggenschwiler JT, Wyler MR, Rakeman AS, Alcorn HL, and Anderson KV (2002). Mouse Dispatched homolog1 is required for long-range, but not juxtacrine, Hh signaling. Curr Biol 12, 1628–1632. [PubMed: 12372258]
22. Ma Y, Erkner A, Gong R, Yao S, Taipale J, Basler K, and Beachy PA (2002). Hedgehog-mediated patterning of the mammalian embryo requires transporter-like function of dispatched. Cell 111, 63–75. 10.1016/S0092-8674(02)00977-7. [PubMed: 12372301]
23. Kawakami T, Kawcak T, Li Y-J, Zhang W, Hu Y, and Chuang P-T (2002). Mouse dispatched mutants fail to distribute hedgehog proteins and are defective in hedgehog signaling. Development 129, 5753–5765. [PubMed: 12421714]
24. Hall ET, Cleverdon ER, and Ogden SK (2019). Dispatching Sonic Hedgehog: Molecular Mechanisms Controlling Deployment. Trends Cell Biol 29, 385–395. 10.1016/j.tcb.2019.02.005. [PubMed: 30852081]
25. Wierbowski BM, Petrov K, Aravena L, Gu G, Xu Y, and Salic A (2020). Hedgehog Pathway Activation Requires Coreceptor-Catalyzed, Lipid-Dependent Relay of the Sonic Hedgehog Ligand. Dev Cell 55, 450. 10.1016/J.DEVCEL.2020.09.017. [PubMed: 33038332]
26. Tukachinsky H, Kuzmickas RP, Jao CY, Liu J, and Salic A (2012). Dispatched and Scube Mediate the Efficient Secretion of the Cholesterol-Modified Hedgehog Ligand. Cell Rep 2, 308–320. 10.1016/j.celrep.2012.07.010. [PubMed: 22902404]
27. Creanga A, Glenn TD, Mann RK, Saunders AM, Talbot WS, and Beachy PA (2012). Scube/You activity mediates release of dually lipid-modified Hedgehog signal in soluble form. Genes Dev 26, 1312–1325. 10.1101/gad.191866.112. [PubMed: 22677548]
28. Li W, Wang L, Wierbowski BM, Lu M, Dong F, Liu W, Li S, Wang P, Salic A, and Gong X (2021). Structural insights into proteolytic activation of the human Dispatched1 transporter for Hedgehog morphogen release. Nature Communications 2021 12:1 12, 1–11. 10.1038/s41467-021-27257-w.
29. Wang Q, Asarnow DE, Ding K, Mann RK, Hatakeyama J, Zhang Y, Ma Y, Cheng Y, and Beachy PA (2021). Dispatched uses Na+ flux to power lipid-modified Hedgehog release. Nature 599, 320. 10.1038/S41586-021-03996-0. [PubMed: 34707294]
30. Lin YC, Roffler SR, Yan YT, and Yang RB (2015). Disruption of Scube2 Impairs Endochondral Bone Formation. Journal of Bone and Mineral Research 30, 1255–1267. 10.1002/JBMR.2451. [PubMed: 25639508]
31. Chen W, Huang H, Hatori R, and Kornberg TB (2017). Essential basal cytonemes take up Hedgehog in the *Drosophila* wing imaginal disc. Development 144, 3134–3144. 10.1242/dev.149856. [PubMed: 28743798]

32. Gradilla A-C, González E, Seijo I, Andrés G, Bischoff M, González-Mendez L, Sánchez V, Callejo A, Ibáñez C, Guerra M, et al. (2014). Exosomes as Hedgehog carriers in cytoneme-mediated transport and secretion. Nat Commun 5, 5649. 10.1038/ncomms6649. [PubMed: 25472772]
33. Coulter ME, Dorobantu CM, Lodewijk GA, Delalande F, Cianferani S, Ganesh VS, Smith RS, Lim ET, Xu CS, Pang S, et al. (2018). The ESCRT-III Protein CHMP1A Mediates Secretion of Sonic Hedgehog on a Distinctive Subtype of Extracellular Vesicles. Cell Rep 24, 973–986.e8. 10.1016/j.celrep.2018.06.100. [PubMed: 30044992]
34. Vyas N, Walvekar A, Tate D, Lakshmanan V, Bansal D, Cicero A. Lo, Raposo G, Palakodeti D, and Dhawan J (2015). Vertebrate Hedgehog is secreted on two types of extracellular vesicles with different signaling properties. Sci Rep 4, 7357. 10.1038/srep07357.
35. Matusek T, Wendler F, Polès S, Pizette S, D'Angelo G, Fürthauer M, and Thérond PP (2014). The ESCRT machinery regulates the secretion and long-range activity of Hedgehog. Nature 516, 99–103. 10.1038/nature13847. [PubMed: 25471885]
36. Hall ET, Dillard ME, Stewart DP, Zhang Y, Wagner B, Levine RM, Pruett-Miller SM, Sykes A, Temirov J, Cheney RE, et al. (2021). Cytoneme delivery of sonic hedgehog from ligand-producing cells requires myosin 10 and a dispatched-boc/cdon co-receptor complex. Elife 10, 1–68. 10.7554/ELIFE.61432.
37. Callejo A, Bilioni A, Mollica E, Gorfinkiel N, Andrés G, Ibáñez C, Torroja C, Doglio L, Sierra J, and Guerrero I (2011). Dispatched mediates Hedgehog basolateral release to form the long-range morphogenetic gradient in the Drosophila wing disk epithelium. Proc Natl Acad Sci U S A 108, 12591–12598. 10.1073/pnas.1106881108. [PubMed: 21690386]
38. Bodeen WJ, Marada S, Truong A, and Ogden SK (2017). A fixation method to preserve cultured cell cytonemes facilitates mechanistic interrogation of morphogen transport. Development 144, 3612–3624. 10.1242/dev.152736. [PubMed: 28827391]
39. Stewart DP, Marada S, Bodeen WJ, Truong A, Sakurada SM, Pandit T, Pruett-Miller SM, and Ogden SK (2018). Cleavage activates dispatched for sonic hedgehog ligand release. Elife 7.
40. Chen H, Liu Y, and Li X (2020). Structure of human Dispatched-1 provides insights into Hedgehog ligand biogenesis. Life Sci Alliance 3. 10.26508/LSA.202000776.
41. Berg JS, and Cheney RE (2002). Myosin-X is an unconventional myosin that undergoes intrafilopodial motility. Nat Cell Biol 4, 246–250. 10.1038/ncb762. [PubMed: 11854753]
42. Hu D, and Marcucio RS (2009). Unique organization of the frontonasal ectodermal zone in birds and mammals. Dev Biol 325, 200–210. 10.1016/J.YDBIO.2008.10.026. [PubMed: 19013147]
43. Lipinski RJ, Holloway HT, O'Leary-Moore SK, Ament JJ, Pecevich SJ, Cofer GP, Budin F, Everson JL, Johnson GA, and Sulik KK (2014). Characterization of Subtle Brain Abnormalities in a Mouse Model of Hedgehog Pathway Antagonist-Induced Cleft Lip and Palate. PLoS One 9, e102603. 10.1371/JOURNAL.PONE.0102603. [PubMed: 25047453]
44. Xavier GM, Seppala M, Barrell W, Birjandi AA, Geoghegan F, and Cobourne MT (2016). Hedgehog receptor function during craniofacial development. Dev Biol 415, 198–215. 10.1016/J.YDBIO.2016.02.009. [PubMed: 26875496]
45. Bernhardt N, Memic F, Velica A, Tran MA, Vieillard J, Sayyab S, Chersa T, Andersson L, Whelan PJ, Boije H, et al. (2022). Hop Mice Display Synchronous Hindlimb Locomotion and a Ventrally Fused Lumbar Spinal Cord Caused by a Point Mutation in Ttc26. eNeuro 9. 10.1523/ENEURO.0518-21.2022.
46. Swiderski RE, Nakano Y, Mullins RF, Seo S, and Bánfi B (2014). A Mutation in the Mouse Ttc26 Gene Leads to Impaired Hedgehog Signaling. PLoS Genet 10, e1004689. 10.1371/JOURNAL.PGEN.1004689. [PubMed: 25340710]
47. Jeong J, and McMahon AP (2005). Growth and pattern of the mammalian neural tube are governed by partially overlapping feedback activities of the hedgehog antagonists patched 1 and Hhip1. Development 132, 143–154. 10.1242/dev.01566. [PubMed: 15576403]
48. Ribes V, Balaskas N, Sasai N, Cruz C, Dessaud E, Cayuso J, Tozer S, Yang LL, Novitch B, Marti E, et al. (2010). Distinct Sonic Hedgehog signaling dynamics specify floor plate and ventral neuronal progenitors in the vertebrate neural tube. Genes Dev 24, 1186. 10.1101/GAD.559910. [PubMed: 20516201]

49. Cohen M, Kicheva A, Ribeiro A, Blassberg R, Page KM, Barnes CP, and Briscoe J (2015). Ptch1 and Gli regulate Shh signalling dynamics via multiple mechanisms. Nature Communications 2015 6:1 6, 1–12. 10.1038/ncomms7709.
50. D'Angelo G, Matusek T, Pizette S, and Thérond PP (2015). Endocytosis of Hedgehog through Dispatched Regulates Long-Range Signaling. Dev Cell 32, 290–303. 10.1016/j.devcel.2014.12.004. [PubMed: 25619925]
51. Giles RH, Ajzenberg H, and Jackson PK (2014). 3D spheroid model of mIMCD3 cells for studying ciliopathies and renal epithelial disorders. Nat Protoc 9, 2725–2731. 10.1038/NPROT.2014.181. [PubMed: 25356583]
52. Etheridge LA, Crawford TQ, Zhang S, and Roelink H (2010). Evidence for a role of vertebrate Disp1 in long-range Shh signaling. Development 137, 133–140. 10.1242/dev.043547. [PubMed: 20023168]
53. Grant BD, and Donaldson JG (2009). Pathways and mechanisms of endocytic recycling. Nature Reviews Molecular Cell Biology 2009 10:9 10, 597–608. 10.1038/nrm2755. [PubMed: 19696797]
54. Ando R, Flors C, Mizuno H, Hofkens J, and Miyawaki A (2007). Highlighted Generation of Fluorescence Signals Using Simultaneous Two-Color Irradiation on Dronpa Mutants. Biophys J 92, L97. 10.1529/BIOPHYSJ.107.105882. [PubMed: 17384059]
55. Rodriguez-Boulan E, and Macara IG (2014). Organization and execution of the epithelial polarity programme. Nature Reviews Molecular Cell Biology 2014 15:4 15, 225–242. 10.1038/nrm3775. [PubMed: 24651541]
56. Von Kleist L, Stahlschmidt W, Bulut H, Gromova K, Puchkov D, Robertson MJ, MacGregor KA, Tomlin N, Pechstein A, Chau N, et al. (2011). Role of the Clathrin Terminal Domain in Regulating Coated Pit Dynamics Revealed by Small Molecule Inhibition. Cell 146, 471–484. 10.1016/J.CELL.2011.06.025. [PubMed: 21816279]
57. Hall ET, Daly CA, Zhang Y, Dillard ME, and Ogden SK (2022). Fixation of Embryonic Mouse Tissue for Cytoneme Analysis. JoVE (Journal of Visualized Experiments), e64100. 10.3791/64100.
58. Muzumdar MD, Tasic B, Miyamichi K, Li N, and Luo L (2007). A global double-fluorescent Cre reporter mouse. Genesis 45, 593–605. 10.1002/DVG.20335. [PubMed: 17868096]
59. Harfe BD, Scherz PJ, Nissim S, Tian H, McMahon AP, and Tabin CJ (2004). Evidence for an Expansion-Based Temporal Shh Gradient in Specifying Vertebrate Digit Identities. Cell 118, 517–528. 10.1016/j.cell.2004.07.024. [PubMed: 15315763]
60. Chamberlain CE, Jeong J, Guo C, Allen BL, and McMahon AP (2008). Notochord-derived Shh concentrates in close association with the apically positioned basal body in neural target cells and forms a dynamic gradient during neural patterning. Development 135, 1097–1106. 10.1242/dev.013086. [PubMed: 18272593]
61. Huang H, Liu S, and Kornberg TB (2019). Glutamate signaling at cytoneme synapses. Science (1979) 363, 948–955. 10.1126/SCIENCE.AAT5053/SUPPL_FILE/AAT5053S9.MOV.
62. Wood BM, Baena V, Huang H, Jorgens DM, Terasaki M, and Kornberg TB (2021). Cytonemes with complex geometries and composition extend into invaginations of target cells. J Cell Biol 220. 10.1083/JCB.202101116.
63. Corbit KC, Aanstad P, Singla V, Norman AR, Stainier DYR, and Reiter JF (2005). Vertebrate Smoothened functions at the primary cilium. Nature 437, 1018–1021. 10.1038/nature04117. [PubMed: 16136078]
64. Rohatgi R, Milenkovic L, and Scott MP (2007). Patched1 regulates hedgehog signaling at the primary cilium. Science 317, 372–376. 10.1126/SCIENCE.1139740. [PubMed: 17641202]
65. Roelink H, Porter JA, Chiang C $, Tanabe Y $, Chang DT, Beachy PA, and Jessellt TM (1995). Floor Plate and Motor Neuron Induction by Different Concentrations of the Amino-Terminal Cleavage Product of Sonic Hedgehog Autoproteolysis. Cell 81, 445–455. [PubMed: 7736596]
66. Ribes V, and Briscoe J (2009). Establishing and interpreting graded Sonic Hedgehog signaling during vertebrate neural tube patterning: the role of negative feedback. Cold Spring Harb Perspect Biol 1. 10.1101/CSHPERSPECT.A002014.

67. Ward L, Pang ASW, Evans SE, and Stern CD (2018). The role of the notochord in amniote vertebral column segmentation. Dev Biol 439, 3. 10.1016/J.YDBIO.2018.04.005. [PubMed: 29654746]
68. Choi KS, Lee C, and Harfe BD (2012). Sonic hedgehog in the notochord is sufficient for patterning of the intervertebral discs. Mech Dev 129, 255–262. 10.1016/J.MOD.2012.07.003. [PubMed: 22841806]
69. Cairns DM, Sato ME, Lee PG, Lassar AB, and Zeng L (2008). A gradient of Shh establishes mutually repressing somitic cell fates induced by Nkx3.2 and Pax3. Dev Biol 323, 152. 10.1016/J.YDBIO.2008.08.024. [PubMed: 18796301]
70. Fitz GN, Weck ML, Bodnya C, Perkins OL, and Tyska MJ (2023). Protrusion growth driven by myosin-generated force. Dev Cell 58, 18–33.e6. 10.1016/J.DEVCEL.2022.12.001. [PubMed: 36626869]
71. Heimsath EG, Yim YI, Mustapha M, Hammer JA, and Cheney RE (2017). Myosin-X knockout is semi-lethal and demonstrates that myosin-X functions in neural tube closure, pigmentation, hyaloid vasculature regression, and filopodia formation. Sci Rep 7, 1–17. 10.1038/s41598-017-17638-x. [PubMed: 28127051]
72. Saalfeld S, Cardona A, Hartenstein V, and Tomančák P (2009). CATMAID: collaborative annotation toolkit for massive amounts of image data. Bioinformatics 25, 1984–1986. 10.1093/BIOINFORMATICS/BTP266. [PubMed: 19376822]
73. Briscoe J, Pierani A, Jessell TM, and Ericson J (2000). A Homeodomain Protein Code Specifies Progenitor Cell Identity and Neuronal Fate in the Ventral Neural Tube. Cell 101, 435–445. 10.1016/S0092-8674(00)80853-3. [PubMed: 10830170]
74. Le Dréau G, and Martí E (2012). Dorsal–ventral patterning of the neural tube: A tale of three signals. Dev Neurobiol 72, 1471–1481. 10.1002/DNEU.22015. [PubMed: 22821665]
75. Zechner D, Müller T, Wende H, Walther I, Taketo MM, Crenshaw EB, Treier M, Birchmeier W, and Birchmeier C (2007). Bmp and Wnt/β-catenin signals control expression of the transcription factor Olig3 and the specification of spinal cord neurons. Dev Biol 303, 181–190. 10.1016/J.YDBIO.2006.10.045. [PubMed: 17150208]
76. Horner VL, and Caspary T (2011). Disrupted dorsal neural tube BMP signaling in the cilia mutant Arl13b hnn stems from abnormal Shh signaling. Dev Biol 355, 43–54. 10.1016/J.YDBIO.2011.04.019. [PubMed: 21539826]
77. Roy S, Huang H, Liu S, and Kornberg TB (2014). Cytoneme-Mediated Contact-Dependent Transport of the Drosophila Decapentaplegic Signaling Protein. Science (1979) 343, 1244624–1244624. 10.1126/science.1244624.
78. Cannac F, Qi C, Falschlunger J, Hausmann G, Basler K, and Korkhov VM (2020). Cryo-EM structure of the Hedgehog release protein Dispatched. Sci Adv 6. 10.1126/SCIADV.AAY7928/SUPPL_FILE/AAY7928_SM.PDF.
79. Brault V, Moore R, Kutsch S, Ishibashi M, Rowitch DH, McMahon AP, Sommer L, Boussadia O, and Kemler R (2001). Inactivation of the β-catenin gene by Wnt1-Cre-mediated deletion results in dramatic brain malformation and failure of craniofacial development. Development 128, 1253–1264. 10.1242/DEV.128.8.1253. [PubMed: 11262227]
80. Cardozo MJ, Sánchez-Arrones L, Sandonis Á, Sánchez-Camacho C, Gestri G, Wilson SW, Guerrero I, and Bovolenta P (2014). Cdon acts as a Hedgehog decoy receptor during proximal-distal patterning of the optic vesicle. Nat Commun 5, 1–13. 10.1038/ncomms5272.
81. Ho EK, and Stearns T (2021). Hedgehog signaling and the primary cilium: Implications for spatial and temporal constraints on signaling. Development (Cambridge) 148. 10.1242/DEV.195552/261696.
82. Kinnebrew M, Iverson EJ, Patel BB, Pusapati GV, Kong JH, Johnson KA, Luchetti G, Eckert KM, McDonald JG, Covey DF, et al. (2019). Cholesterol accessibility at the ciliary membrane controls hedgehog signaling. Elife 8. 10.7554/ELIFE.50051.
83. Raleigh DR, Sever N, Choksi PK, Sigg MA, Hines KM, Thompson BM, Elnatan D, Jaishankar P, Bisignano P, Garcia-Gonzalo FR, et al. (2018). Cilia-Associated Oxysterols Activate Smoothened. Mol Cell 72, 316–327.e5. 10.1016/J.MOLCEL.2018.08.034. [PubMed: 30340023]

84. Deshpande I, Liang J, Hedeen D, Roberts KJ, Zhang Y, Ha B, Latorraca NR, Faust B, Dror RO, Beachy PA, et al. (2019). Smoothened stimulation by membrane sterols drives Hedgehog pathway activity. Nature 2019 571:7764 571, 284–288. 10.1038/s41586-019-1355-4. [PubMed: 31263273]
85. Kinnebrew M, Luchetti G, Sircar R, Frigui S, Viti LV, Naito T, Beckert F, Saheki Y, Siebold C, Radhakrishnan A, et al. (2021). Patched 1 reduces the accessibility of cholesterol in the outer leaflet of membranes. Elife 10. 10.7554/ELIFE.70504.
86. Sentmanat MF, Peters ST, Florian CP, Connelly JP, and Pruett-Miller SM (2018). A Survey of Validation Strategies for CRISPR-Cas9 Editing. Sci Rep 8, 888. 10.1038/s41598-018-19441-8. [PubMed: 29343825]
87. Connelly JP, and Pruett-Miller SM (2019). CRIS.py: A Versatile and High-throughput Analysis Program for CRISPR-based Genome Editing. Sci Rep 9, 1–8. 10.1038/s41598-019-40896-w. [PubMed: 30626917]
88. Zheng M, Karki R, Kancharana B, Berns H, Pruett-Miller SM, and Kanneganti TD (2021). Caspase-6 promotes activation of the caspase-11-NLRP3 inflammasome during gram-negative bacterial infections. J Biol Chem 297. 10.1016/J.JBC.2021.101379.
89. Brooks SP, Pask T, Jones L, and Dunnett SB (2004). Behavioural profiles of inbred mouse strains used as transgenic backgrounds. I: motor tests. Genes Brain Behav 3, 206–215. 10.1111/J.1601-183X.2004.00072.X. [PubMed: 15248866]
90. Abler LL, Mehta V, Keil KP, Joshi PS, Flucus CL, Hardin HA, Schmitz CT, and Vezina CM (2011). A high throughput in situ hybridization method to characterize mRNA expression patterns in the fetal mouse lower urogenital tract. Journal of Visualized Experiments 54, 2912. 10.3791/2912.
91. Schindelin J, Arganda-Carreras I, Frise E, Kaynig V, Longair M, Pietzsch T, Preibisch S, Rueden C, Saalfeld S, Schmid B, et al. (2012). Fiji: An open-source platform for biological-image analysis. Nat Methods 9, 676–682. 10.1038/nmeth.2019. [PubMed: 22743772]
92. Kaufmann MH (1992). The Atlas of Mouse Development [Hardcover].
93. Sloan TFW, Qasaimeh MA, Juncker D, Yam PT, and Charron F (2015). Integration of Shallow Gradients of Shh and Netrin-1 Guides Commissural Axons. PLoS Biol 13, e1002119. 10.1371/JOURNAL.PBIO.1002119. [PubMed: 25826604]
94. Hall E, and Ogden S (2018). Preserve Cultured Cell Cytonemes through a Modified Electron Microscopy Fixation. Bio Protoc 8. 10.21769/BioProtoc.2898.
95. Berg S, Kutra D, Kroeger T, Straehle CN, Kausler BX, Haubold C, Schiegg M, Ales J, Beier T, Rudy M, et al. (2019). ilastik: interactive machine learning for (bio)image analysis. Nature Methods 2019 16:12 16, 1226–1232. 10.1038/s41592-019-0582-9. [PubMed: 31570887]
96. Subramanian A, Tamayo P, Mootha VK, Mukherjee S, Ebert BL, Gillette MA, Paulovich A, Pomeroy SL, Golub TR, Lander ES, et al. (2005). Gene set enrichment analysis: A knowledge-based approach for interpreting genome-wide expression profiles. Proc Natl Acad Sci U S A 102, 15545–15550. 10.1073/PNAS.0506580102/SUPPL_FILE/06580FIG7.JPG. [PubMed: 16199517]
97. Schneider-Mizell CM, Gerhard S, Longair M, Kazimiers T, Li F, Zwart MF, Champion A, Midgley FM, Fetter RD, Saalfeld S, et al. (2016). Quantitative neuroanatomy for connectomics in Drosophila. Elife 5. 10.7554/ELIFE.12059.
98. Yost EA, Mervine SM, Sabo JL, Hynes TR, and Berlot CH (2007). Live cell analysis of G protein beta5 complex formation, function, and targeting. Mol Pharmacol 72, 812–825. 10.1124/MOL.107.038075. [PubMed: 17596375]
99. Zhao Y, Araki S, Wu J, Teramoto T, Chang Y-F, Nakano M, Abdelfattah AS, Fujiwara M, Ishihara T, Nagai T, et al. (2011). An expanded palette of genetically encoded Ca^{2+} indicators. Science 333, 1888–1891. 10.1126/science.1208592. [PubMed: 21903779]
100. Marada S, Navarro G, Truong A, Stewart DP, Arensdorf AM, Nachtergaele S, Angelats E, Opferman JT, Rohatgi R, McCormick PJ, et al. (2015). Functional Divergence in the Role of N-Linked Glycosylation in Smoothened Signaling. PLoS Genet 11. 10.1371/JOURNAL.PGEN.1005473.
101. Ogden SK, Ascano M, Stegman MA, Suber LM, Hooper JE, and Robbins DJ (2003). Identification of a Functional Interaction between the Transmembrane Protein

Smoothened and the Kinesin-Related Protein Costal2. Current Biology 13, 1998–2003. 10.1016/J.CUB.2003.10.004. [PubMed: 14614827]

102. McQuin C, Goodman A, Chernyshev V, Kamentsky L, Cimini BA, Karhohs KW, Doan M, Ding L, Rafelski SM, Thirstrup D, et al. (2018). CellProfiler 3.0: Next-generation image processing for biology. PLoS Biol 16, e2005970. 10.1371/journal.pbio.2005970. [PubMed: 29969450]
103. Sasaki H, Hui CC, Nakafuku M, and Kondoh H (1997). A binding site for Gli proteins is essential for HNF-3beta floor plate enhancer activity in transgenics and can respond to Shh in vitro. Development 124, 1313–1322. 10.1242/DEV.124.7.1313. [PubMed: 9118802]
104. Chen JK, Taipale J, Cooper MK, and Beachy PA (2002). Inhibition of Hedgehog signaling by direct binding of cyclopamine to Smoothened. Genes Dev 16, 2743–2748. 10.1101/gad.1025302. [PubMed: 12414725]

Highlights

- Dispatched cleavage promotes Sonic Hedgehog endocytic recycling and cytoneme loading.
- Cytonemes contribute to Sonic Hedgehog deployment during neurodevelopment.
- Myosin 10 promotes formation of neuronal cytonemes for SHH and WNT transport.
- Cytoneme dysfunction compromises neuronal cell fate specification.

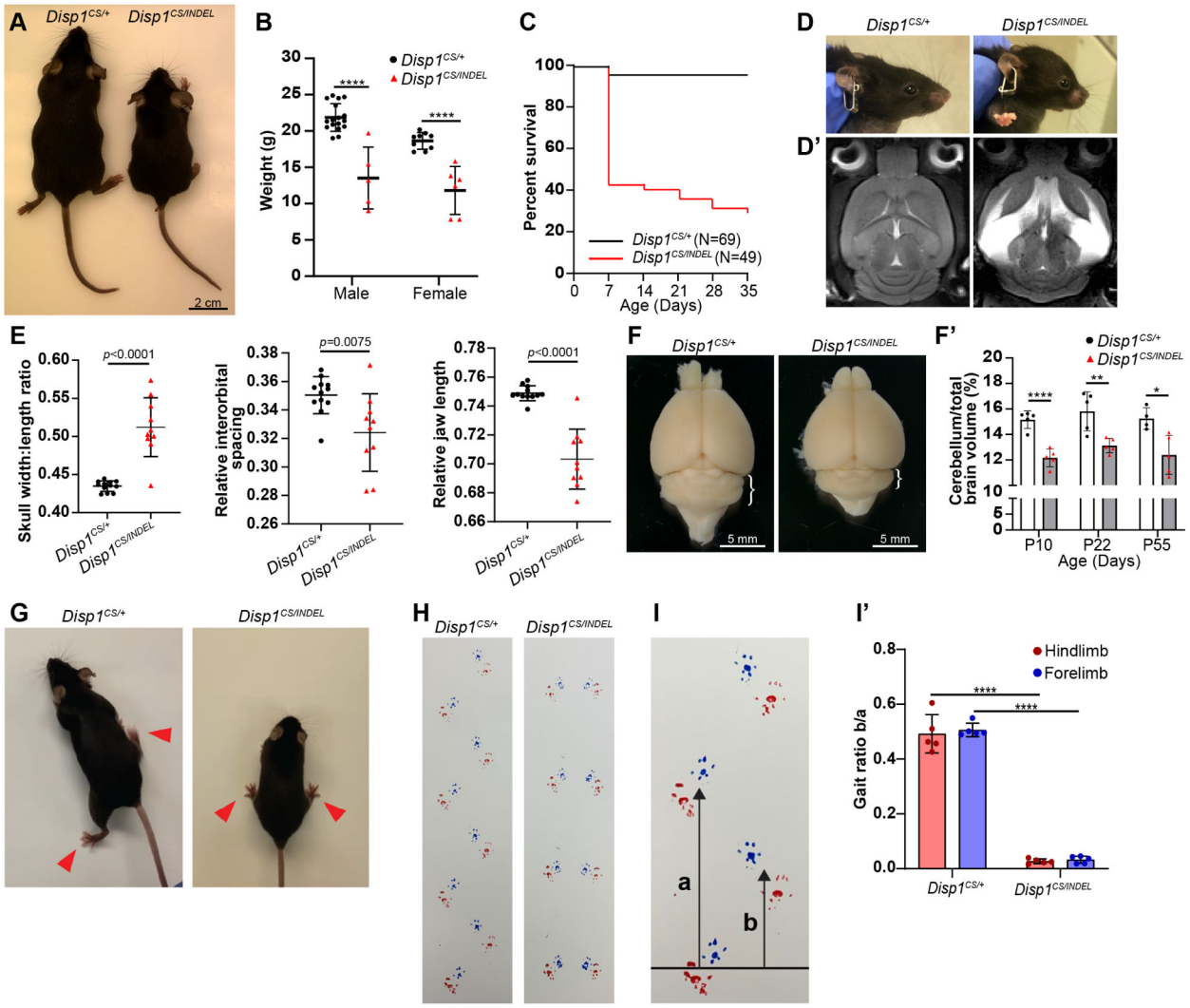

Figure 1: DISP cleavage disruption triggers developmental defects.

(**A-B**) Male and female *Disp1*$^{CS/INDEL}$ mice are reduced in size (n=5-17 mice/genotype). P35 female mice are shown in (**A**). (**C**) A Kaplan-Meier survival curve shows reduced viability of *Disp1*$^{CS/INDEL}$ mice. Sixteen litters were monitored weekly from P0 to P35. (**D-E**) *Disp1*$^{CS/INDEL}$ mice have hydrocephalus and craniofacial defects. (**E**) CT scans of *Disp1*$^{CS/INDEL}$ skulls show expanded width to length ratios, reduced interorbital spacing, and reduced jaw length (n=10-12 mice/genotype). (**F-F'**) *Disp1*$^{CS/INDEL}$ mice have small cerebella (brackets). Cerebellum volume relative to total brain volume was calculated at P0, P22 and P55. At least 4 mice of each genotype were analyzed. (**G-I'**) *Disp1*$^{CS/INDEL}$ mice have a hopping gait. (**H-I**) Forelimbs (blue) and hindlimbs (red) were painted to track limb placement and quantify gait ratios. Gait ratios were calculated from 5 mice/genotype with male and female data pooled. All data are represented as mean ± SD, *p<0.05, **p<0.01, ****p<0.0001. See Figure S1 and Movie 1.

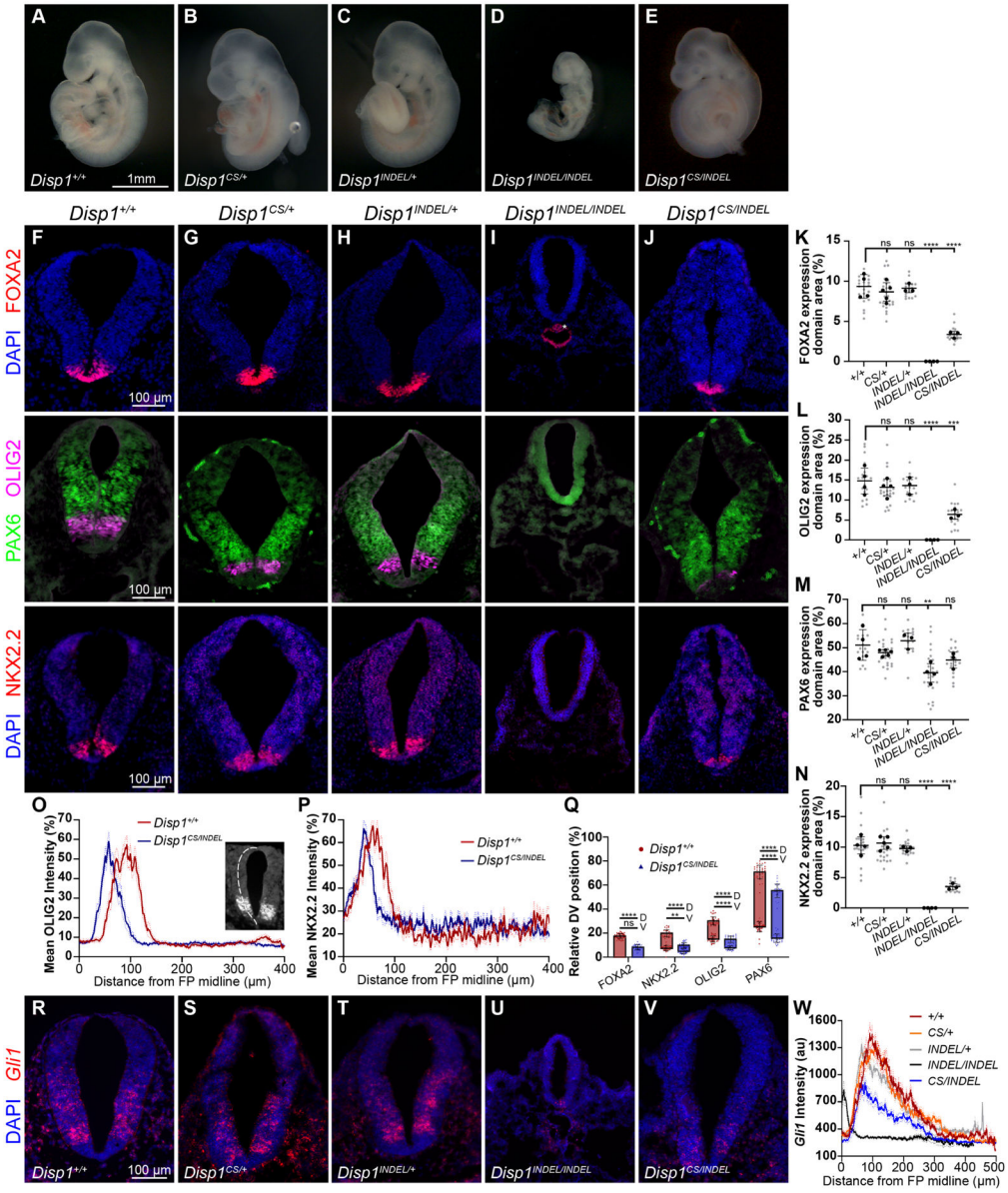

Figure 2: DISP cleavage disruption alters neural tube patterning.

(**A-E**) E9.5/27-29 somite embryos of the indicated genotypes are shown. (**F-J**) Cardiac level sections of developing neural tubes of E9.5/27-29 somite embryos were stained for floor plate and ventral progenitor markers. DAPI marks nuclei. Asterisk denotes FOXA2 expression in the notochord and foregut (**I**). (**K-N**) Mean expression domain areas of the indicated progenitor markers in neural tube sections analyzed from n=3-5 embryos per genotype (black dots). Grey dots represent individual sections. (**O-P**) Mean fluorescence intensity line plots along the dorsal/ventral (DV) axis are shown for OLIG2 (**O**) and NKX2.2 (**P**). Line plots were measured from the basal surface of the floorplate (FP) midline to roofplate (dotted line, inset in **O**). Dotted lines indicate SEM. n=14-18 total sections from 3 embryos per genotype. (**Q**) Box plots of the D/V positions of the indicated progenitor domains relative to neural tube length. Ventral and dorsal domains positions are shown at

box tops and bottoms, respectively. n=3 embryos with 5-8 sections per embryo. The floor plate midline is set to zero. (**R-V**) RNAScope *Gli1 in situ* hybridization in E9.5/25-30 somite stage matched cardiac level neural tube sections. *Gli1* probe is red and DAPI is blue. (**W**) Mean *Gli1* signal intensity plots from the floor plate toward the roof plate. Three embryos per genotype with n=26-30 sections per genotype quantified. Dotted lines indicate SEM. Scatter and box plot data are represented as mean ± SD, **p<0.01, ***p<0.01, ****p<0.0001, ns= not significant. See Figure S2.

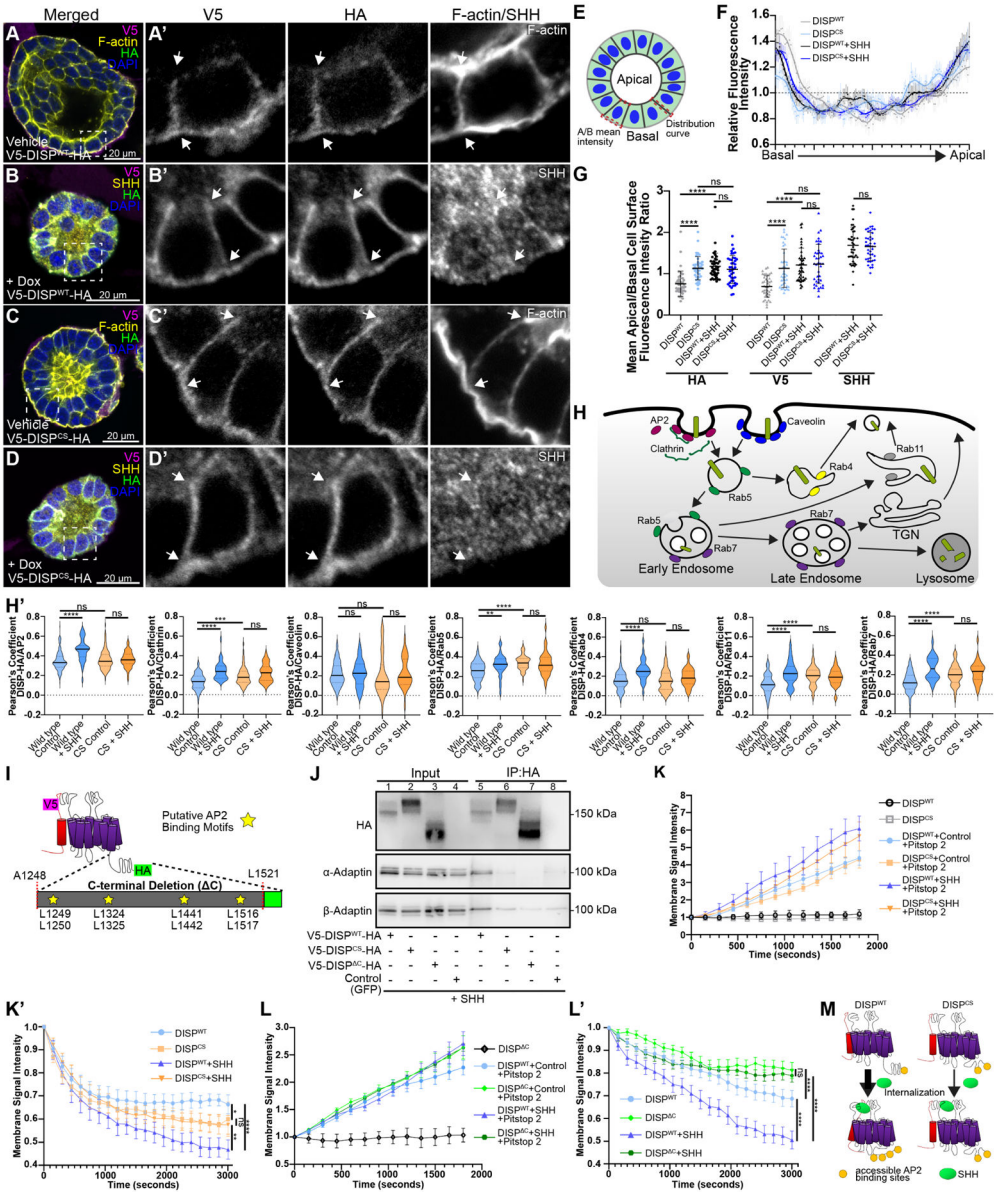

Figure 3: DISP cleavage promotes SHH-stimulated endocytic recycling.

(**A-D'**) IMCD3 spheroids stably expressing DISP^{WT} or DISP^{CS} proteins were immunostained with anti-V5 (magenta) and anti-HA (green). F-actin is yellow in **A** and **C** (doxycycline negative) and doxycycline-induced SHH is yellow in **B** and **D**. DAPI is blue. Zoom regions are indicated by the dashed lines. Arrows indicate areas analyzed for **F-G**. (**E**) A model of an IMCD3 spheroid indicates areas of analysis for the distribution curve in (**F**) and apical/basal fluorescent intensity ratios (**G**). (**F**) Average fluorescence intensity distribution curve of V5-DISP-HA from basal to apical membranes is shown. Data are normalized as average distribution intensity equal to 1 with dots representing mean intensity across the distribution of the cell ±SEM (n=21-29 cells). Solid lines represent the integrated curve of fluorescence intensity across the cell. (**G**) Mean fluorescence intensity ratios (apical/basal) of HA, V5, and SHH in DISP^{WT} or DISP^{CS} expressing spheroid cells

are shown (n=40-47 cells per condition). (**H**) Summary diagram of clathrin and caveolin endocytic pathways. (**H'**) Pearson's correlation coefficient values for colocalization between DISP-HA and endosomal markers in *Disp*^{KO} MEFs stably expressing V5-DISP^{WT}-HA or V5-DISP^{CS}-HA in the presence of SHH-mCherry (n= 23-39 cells) or empty vector control (n= 60-126 cells). Data are shown as the median (solid line) with 1st and 3rd quartiles (dotted lines). (**I**) Schematic of V5-DISP-HA protein with candidate dileucine AP2 binding motifs and carboxyl-terminal deletion that eliminates the sites. (**J**) Co-immunoprecipitation of DISP-HA from membrane fractions from *Disp*^{KO} MEFs stably expressing SHH with the indicated V5-DISP-HA proteins or GFP control western blotted for clathrin adaptor subunits. (**K-L'**) Plasma membrane fluorescence intensity plots are shown for the indicated DISP-Dronpa3 proteins expressed in MDCK cell monolayers in the presence of Pitstop 2 (**K** and **L**) and following Pitstop 2 washout (**K'** and **L'**). Cells co-express membrane-mCherry (control) or SHH-mCherry. n=3 experiments with 31-54 cells analyzed per condition. Data are represented as mean +/− 95% confidence interval. (**M**) A model for DISP internalization. DISP cleavage by Furin promotes SHH-induced conformation shifts that enhance DISP-AP2 association for clathrin-mediated endocytosis of SHH-DISP complexes. Cleavage disruption alters DISP conformation to elevate basal internalization and attenuate SHH-stimulated internalization. For all experiments, significance is indicated by *p<0.05, **p<0.01, ***p<0.001, ****p<0.0001, ns = not significant. See Figure S3.

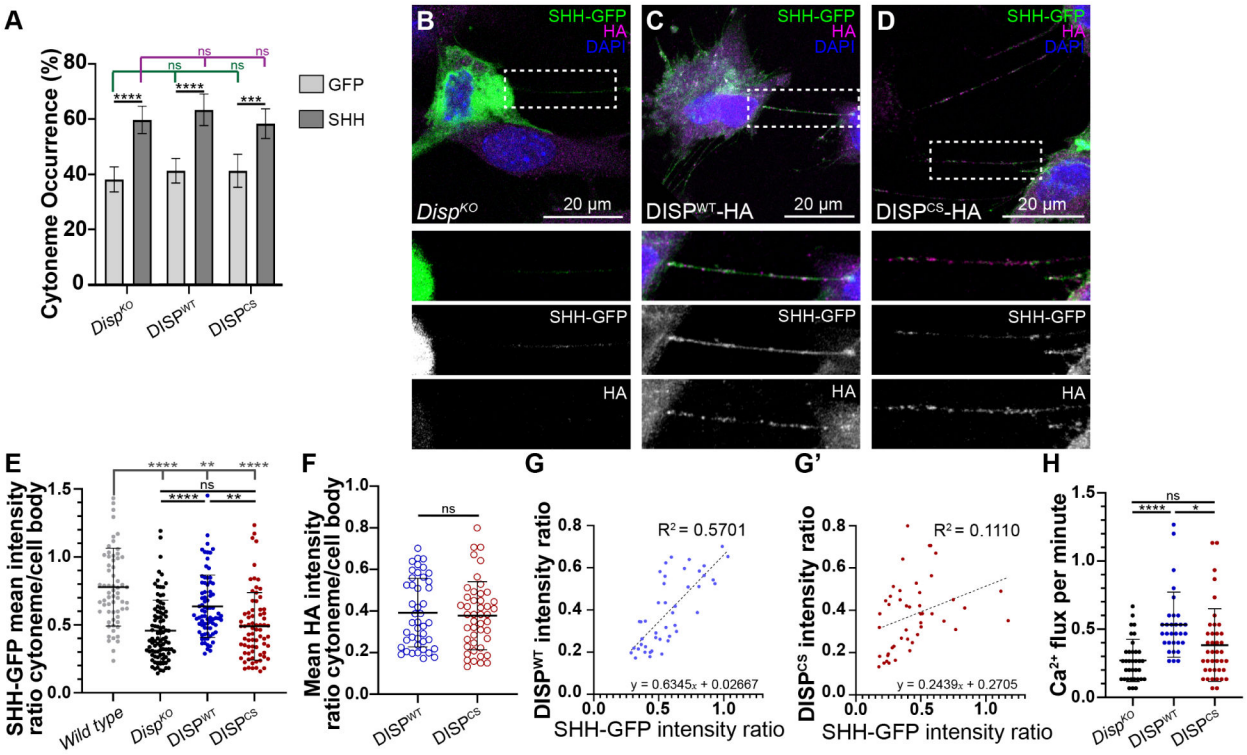

Figure 4: DISP cleavage promotes SHH cytoneme entry and signaling.

(**A**) Cytoneme occurrence rates are shown for *Disp*^{KO} MEFs stably expressing the indicated DISP proteins with GFP control (light gray) or SHH-GFP (dark gray). (**B-D**) Confocal images of *Disp*^{KO} MEFs expressing SHH-GFP (green), with stably expressed V5-DISP^{WT}-HA (**C**, magenta) or V5-DISP^{CS}-HA (**D,** magenta) are shown. Zoom images show regions outlined in the upper panels. (**E-F**) Scatter plots are shown for mean SHH-GFP (**E**) or DISP (**F**) cytoneme/cell body signal intensity ratios. (**G-G'**) Linear regression models of the relative intensity of SHH-GFP to DISP-HA per individual cytoneme in V5-DISP^{WT}-HA or V5-DISP^{CS}-HA expressing *Disp*^{KO} MEFs. (**H**) NIH-3T3 cells expressing the R-GECO Ca^{2+} reporter were co-cultured with control or DISP-expressing *Disp*^{KO} cells as indicated. Flux rates per minute were calculated from n=31-41 individual cells in contact with cytonemes from SHH-GFP producing *Disp*^{KO} control or DISP^{WT}/DISP^{CS} expressing MEFs. Data are represented as mean ± SD. For all graphs, significance indicated as *p<0.05, **p<0.01, ***p<0.001, ****p<0.0001, ns = not significant.

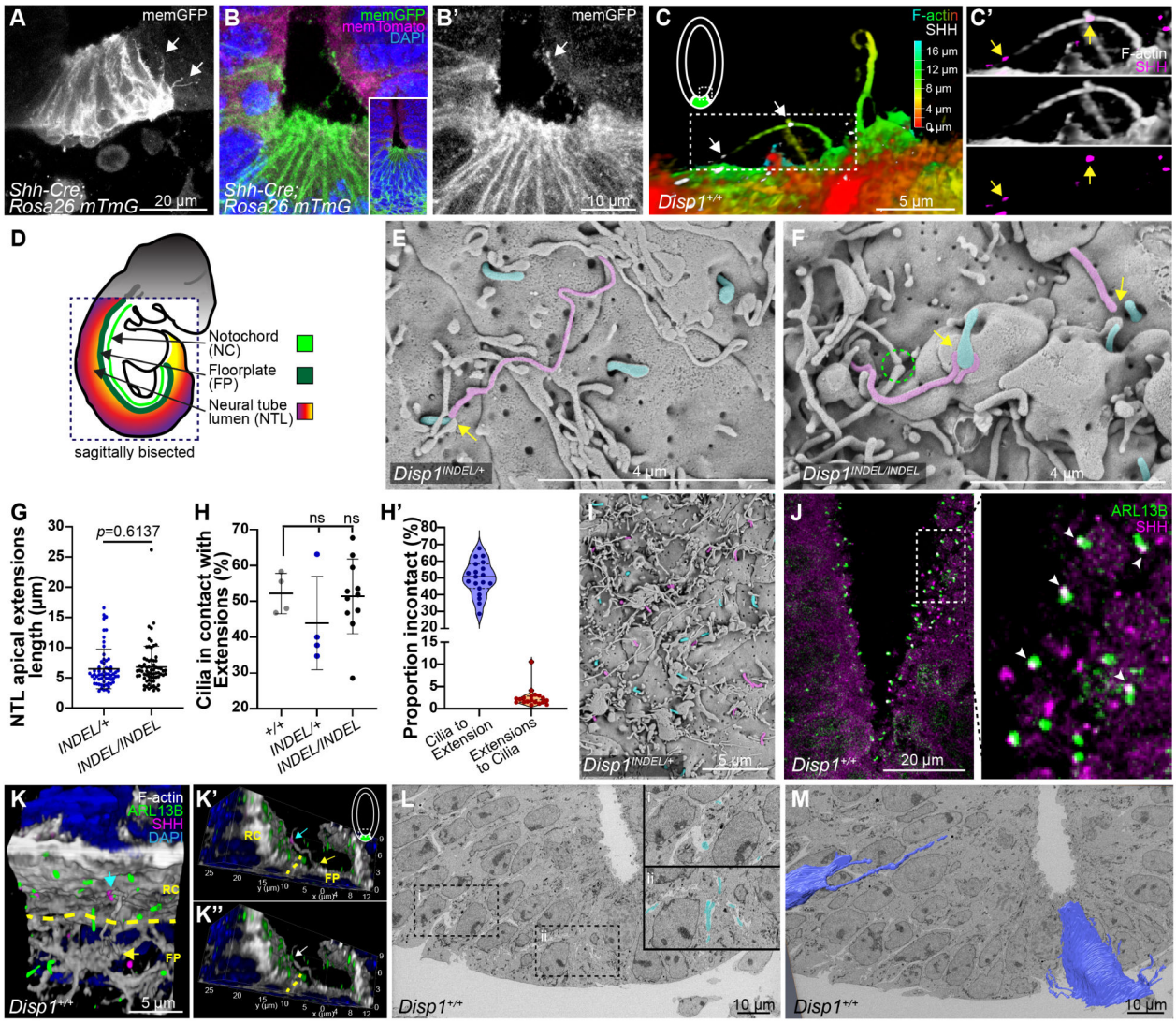

Figure 5: SHH localizes to cytonemes in the developing neural tube.

(**A-B'**) Neural tubes are shown of E9.5/25-30 somite *SHH-Cre;Rosa26*$^{mT/mG}$ embryos. (**A**) GFP-labeled cellular extensions originating from *Shh*-expressing cells of the floor plate were detected in 69/78 section scans from 17 embryos. (**B-B'**) GFP-positive membrane extensions from the floor plate reach across the neural tube lumen to contact adjacent cells (inset shows zoom out). (**C-C'**) A 3D render shows extensions from the neural tube floor plate of a *Disp1*$^{+/+}$ E9.5 embryo stained for F-actin (depth shaded in **C**, white in **C'**) and anti-SHH (white, arrows in **C**, magenta in **C'**). The area rendered in the figure is indicated by the dashed box in the neural tube schematic. An average of 11 neural tube lumen extensions like those in **B** and **C** were observed per tissue section analyzed. n= 976 extensions scored across 32 embryos. (**D**) Schematic of a sagittally bisected embryo showing locations of the apical surface of the neural tube lumen (NTL), the floor plate (FP), and notochord (NC). (**E-F**) SEM images of E9.5 (**E**) *Disp1*$^{INDEL/+}$ and (**F**) *Disp1*$^{INDEL/INDEL}$ NTL. Apical extensions (magenta) contact primary cilia (arrows, blue), or make cytoneme tip-to-tip contact (dotted circle). (**G**) Scatter plot of lengths of NTL

apical extensions. Three embryos per genotype were examined. A total of 61 (*Disp1*$^{INDEL/+}$) and 68 (*Disp1*$^{INDEL/INDEL}$) extensions were measured. (**H**) Percentage of cilia observed contacting cellular extensions per scan. Four to 11 scans were analyzed per genotype with n=344 *Disp1*$^{+/+}$, n=684 *Disp1*$^{INDEL/+}$, and n=756 *Disp1*$^{INDEL/INDEL}$ ciliary contacts scored. ns = not significant. (**H'**) Violin plots indicate proportions of cilia in contact with extensions and extensions in contact with primary cilia across all genotypes analyzed. n=1784 primary cilia and 39,070 total extensions scored. (**I**) Representative image of cilia to extension contacts. Cilia contacting extensions are shaded pink and cilia not contacting extensions are shaded blue. (**J**) E9.0/17-20 somite *Disp1*$^{+/+}$ neural tubes immunostained for ARL13B (green) and SHH (magenta). Arrowheads indicate SHH puncta near primary cilia. n=10 embryos. (**K-K"**) 3D render of a *Disp1*$^{+/+}$ ventral neural tube shown in two orientations. An F-actin (white) labeled extension originating from the floor plate (FP, yellow arrow) with SHH (magenta) contacts an ARL13B (green) labeled primary cilium of a receiving cell (RC, blue arrow). Yellow dotted line marks FP and RC division. Area rendered is indicated by the dashed box. (**L**) A single SBF-SEM section of an E9.5 *Disp1*$^{+/+}$ neural tube floor plate shows intercellular gaps that contain isolated 'blebs' (blue, inset i) and partial extensions (inset ii). (**M**) 3D reconstruction of membrane extensions from two cells traced across multiple segments. See Figure S4 and Movies 3-4.

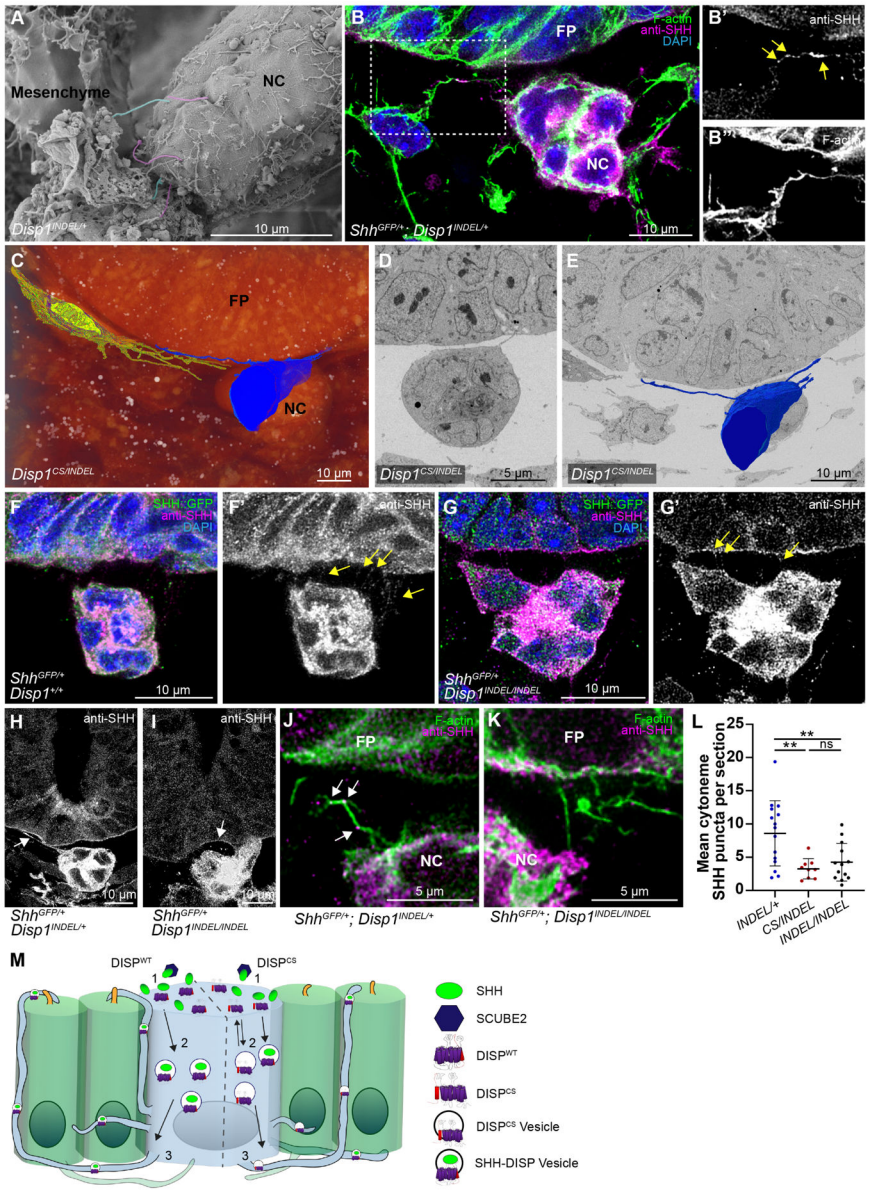

Figure 6: SHH-containing cytonemes connect the notochord, neural tube floor plate, and surrounding mesenchyme.

(**A**) SEM of an E9.5 *Disp1*$^{INDEL/+}$ embryo shows the notochord (NC) and mesenchyme. NC-derived extensions (magenta) reach toward mesenchymal cell extensions (blue). (**B-B”**) E9.5 *Shh*$^{GFP/+}$*;Disp1*$^{INDEL/+}$ embryo stained for SHH (magenta), F-actin (green), and DAPI (blue). SHH puncta (**B’**, arrows) are visible on F-actin-positive (**B”**) extensions between the mesenchyme and NC. The floor plate (FP) is shown at top, a mesenchymal cell is left and the NC is right. (**C-E**) 3D volume render of a single NC cell (blue) with an extension contacting extensions from a mesenchymal cell (yellow). The same cell sends extensions to the basal surface of the neural tube FP (single section shown in **D** and 3D volume render in **E**). See Figure S5A-B and Movie 5. (**F-G’**) E9.5/27-29 somite embryos from the indicated genotypes were immunostained for anti-GFP (green), anti-SHH (magenta), and DAPI (blue). Linear tracks of SHH are visible between the NC

and FP (**F', G'** yellow arrows). (**H**) Anti-SHH-positive extensions from the NC (arrow) contact the basal surface of cells near the edge of the *Shh*-expressing neural tube FP in $Shh^{GFP/+};Disp1^{INDEL/+}$ E9.5 embryos. (**I**) SHH signal is detected along the basal surface of a $Shh^{GFP/+};Disp1^{INDEL/INDEL}$ neural tube (arrow), but signal in the FP is reduced. (**J-K**) Anti-SHH puncta (magenta, arrows) are on F-actin-positive (green) extensions between the NC and FP in $Shh^{GFP/+};Disp1^{INDEL/+}$ embryos (**J**). Few SHH puncta are evident in connections between the NC and FP in $Shh^{GFP/+};Disp1^{INDEL/INDEL}$ embryos (**K**). (**L**) Scatter plot of mean anti-SHH puncta per scan area in notochord-to-floor plate cytonemes for $Shh^{GFP/+};Disp1^{INDEL/+}$, $;Disp1^{CS/INDEL}$, and $Disp1^{INDEL/INDEL}$ embryo sections. At least 2 embryos per genotype with 9-15 sections per genotype were analyzed. Data are represented as mean ± SD. **p<0.01, ns = not significant. (**M**) Model for how endocytosis promotes DISP-SHH entry into cytonemes. Both wild type and cleavage deficient DISP proteins enter cytonemes, but only wild type DISP efficiently transports SHH into them. See Figure S5.

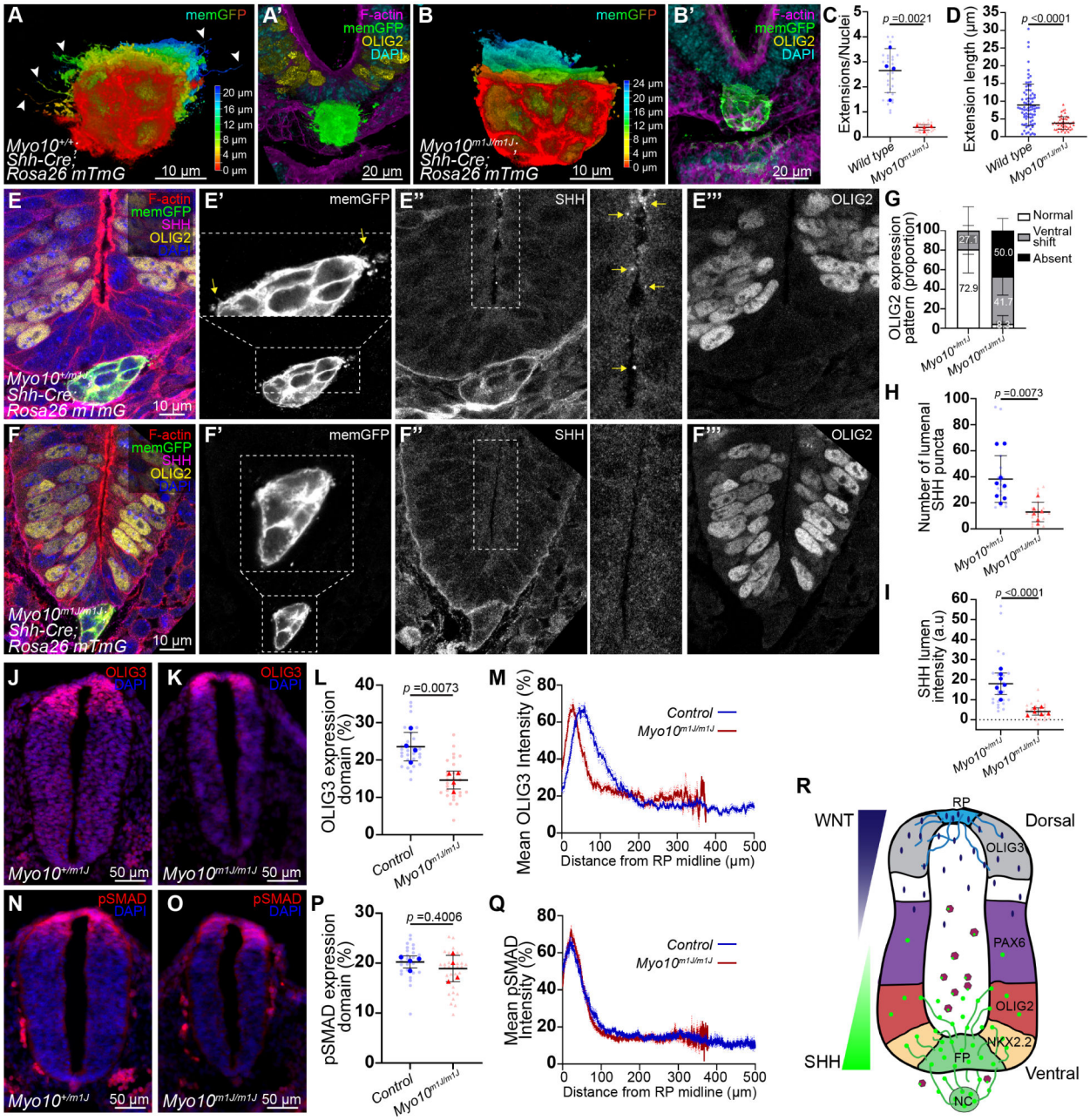

Figure 7: Myosin 10 promotes cytoneme formation and SHH and WNT signaling *in vivo*.

(**A-B'**) 3D renders of ventral neural tubes and depth shaded notochords with extensions (arrowheads) from E8.5/10 somite *SHH-Cre;Rosa26*$^{mT/mG}$ *Myo10*$^{+/+}$ (**A-A'**) and *Myo10*$^{m1J/m1J}$ (**B-B'**) embryos. Notochords are green in **A'** and **B'**. (**A',B'**) Tissue stained for OLIG2 (yellow), F-actin (magenta), anti-GFP (green), and DAPI (cyan). n=4-6 embryos per genotype analyzed. (**C-D**) Scatter plots indicate extensions per nuclei (**C**) and extension lengths (**D**), quantified from SBF-SEM of E9.5 neural tube floor plates from 4 individual *Myo10*$^{+/+}$ and 2 *Myo10*$^{m1J/m1J}$ embryos with 2 scan series per embryo. Large dots/triangles represent individual scan series. Small markers indicate individual sections. (**E-F'"**) E8.5/14 somite *SHH-Cre;Rosa26*$^{mT/mG}$ (**E**) *Myo10*$^{+/m1J}$ and (**F**) *Myo10*$^{m1J/m1J}$ notochord and

neural tube sections with SHH (magenta), OLIG2 (yellow), F-actin (red) GFP (green), and DAPI (blue). *Myo10*$^{+/m1J}$ embryos exhibit notochord-derived extensions (**E'** arrows) and neural tube luminal SHH puncta (**E"**, zoom in arrows). (**G**) The proportion of tissue sections with normal, ventrally shifted, or absent OLIG2 from E8.5/10-15 somite *Myo10*$^{+/m1J}$ (n=8) and *Myo10*$^{m1J/m1J}$ (n=3) embryos are shown. Three to 6 sections were analyzed per embryo, error bars = SD. (**H-I**) Quantification of neural tube lumen SHH puncta (**H**) and SHH signal intensity across the apical surface of the lumen (**I**) is shown. Large dots/triangles represent individual embryos. Translucent markers indicate individual sections. n=6-8 embryos per genotype at the 10-15 somite stage. (**J-Q**) MYO10 loss compromises dorsal neural tube WNT signaling. E9.5/25-30 somite *Myo10*$^{+/m1J}$ and *Myo10*$^{m1J/m1J}$ neural tube sections stained for OLIG3 (red) (**J-K**) or pSMAD (red) (**N-O**) with DAPI (blue). (**L,P**) Mean expression domain areas of 4 Control (2 *Myo10*$^{+/+}$ and 2 *Myo10*$^{+/m1J}$) and 4 *Myo10*$^{m1J/m1J}$ somite stage matched embryos. Large dots/triangles represent individual embryos. Small markers indicate individual sections. Scatter plot data represented as mean ± SD. (**M,Q**) Mean fluorescence intensity line plots along the dorsal/ventral (DV) axis are shown for OLIG3 (**M**) and pSMAD (**Q**). Dotted lines indicate SEM. n=21-25 total sections from 4 embryos per genotype. See Figure S6 and S7. (**R**) A model for cytoneme-based signal transport in the neural tube. Cytonemes assist in deployment of WNT (blue) from the roof plate and SHH (green) from the notochord and floor plate. Cytoneme-based transport likely collaborates with SCUBE2 assisted diffusion of SHH (magenta/green luminal complexes) and free diffusion of WNT (blue dots) to refine or reinforce the morphogen signaling gradients during neural tube development.

Key resources table

REAGENT or RESOURCE	SOURCE	IDENTIFIER
Antibodies		
Chicken polyclonal anti-GFP	Aves	Cat# GFP-1020; RRID:AB_10000240
Mouse monoclonal anti-Pax6	DSHB	Cat# pax6; RRID:AB_528427
Rabbit polyclonal anti-Olig2	Millipore	Cat# AB9610; RRID:AB_570666
Rabbit polyclonal anti-FOXA2	Abcam	Cat# ab108422; RRID:AB_11157157
Rabbit polyclonal anti-Nkx2.2	Novus	Cat# NBP1-82554; RRID:AB_11005513
Mouse monoclonal anti-SHH (supernatant)	DSHB	Cat# 5E1; RRID:AB_528466
Rabbit polyclonal anti-ARL13B	Proteintech	Cat# 17711-1-AP; RRID:AB_2060867
Rabbit polyclonal anti-SHH (H160)	Santa Cruz Biotechnology	Cat# sc-9024; RRID:AB_2239216
Rat monoclonal anti-HA (clone 3F10)	Roche	Cat# 11867423001; RRID:AB_390918
Rabbit monoclonal anti-Phospho-Smad1 (Ser463/465)/Smad5 (Ser463/465)/Smad9 (Ser465/467) (D5B10)	Cell Signaling Technology	Cat# 13820; RRID:AB_2493181
Rabbit monoclonal anti-OLIG3 (JE56-40)	Thermo Fisher Scientific	Cat# MA5-44904; RRID:AB_2931360
Mouse monoclonal anti-V5 tag (SV5-Pk1) (formally #46-0705)	Thermo Fisher Scientific	Cat# R960-25; RRID:AB_2556564
Mouse monoclonal anti-Rab5 (E6N8S)	Cell Signaling Technology	Cat# 46449; RRID:AB_2799303
Rabbit monoclonal anti-Rab7 (D95F2)	Cell Signaling Technology	Cat# 9367; RRID:AB_1904103
Rabbit monoclonal anti-Rab11 (D4F5)	Cell Signaling Technology	Cat# 5589; RRID:AB_10693925
Rabbit polyclonal anti-Rab4	Thermo Fisher Scientific	Cat# PA3-912; RRID:AB_2269382
Rabbit monoclonal anti-Caveolin-1 (D46G3)	Cell Signaling Technology	Cat# 3267; RRID:AB_2275453
Rabbit monoclonal anti-Clathrin Heavy Chain (D3C6)	Cell Signaling Technology	Cat# 4796; RRID:AB_10828486
Mouse monoclonal anti-alpha Adaptin	Thermo Fisher Scientific	Cat# MA3-061; RRID:AB_2056321
Rabbit monoclonal anti-SHH (C9C5)	Cell Signaling Technology	Cat# 2207; RRID:AB_2188191
Rabbit monoclonal anti-KIF5B	Abcam	Cat# ab167429; RRID:AB_2715530
Mouse monoclonal anti-alpha-Tubulin (DM1A)	Cell Signaling Technology	Cat# 3873; RRID:AB_1904178
Rabbit polyclonal anti-Beta-2-adaptin	Bethyl	Cat# A304-718A; RRID:AB_2620913
Goat anti-Mouse IgG (H+L) Highly Cross-Adsorbed Secondary Antibody, Alexa Fluor™ 488	Thermo Fisher Scientific	Cat# A-11029; RRID:AB_2534088
Goat anti-Rabbit IgG (H+L) Highly Cross-Adsorbed Secondary Antibody, Alexa Fluor™ 488	Thermo Fisher Scientific	Cat# A-11034; RRID:AB_2576217
Goat anti-Rat IgG (H+L) Cross-Adsorbed Secondary Antibody, Alexa Fluor™ 488	Thermo Fisher Scientific	Cat# A-11006; RRID:AB_2534074
Goat anti-Mouse IgG (H+L) Highly Cross-Adsorbed Secondary Antibody, Alexa Fluor™ 555	Thermo Fisher Scientific	Cat# A-21424; RRID:AB_141780

REAGENT or RESOURCE	SOURCE	IDENTIFIER
Goat anti-Rabbit IgG (H+L) Highly Cross-Adsorbed Secondary Antibody, Alexa Fluor™ 555	Thermo Fisher Scientific	Cat# A-21429; RRID:AB_2535850
Goat anti-Rat IgG (H+L) Cross-Adsorbed Secondary Antibody, Alexa Fluor™ 555	Thermo Fisher Scientific	Cat# A-21434; RRID:AB_2535855
Goat anti-Mouse IgG (H+L) Highly Cross-Adsorbed Secondary Antibody, Alexa Fluor™ 647	Thermo Fisher Scientific	Cat# A-21236; RRID:AB_2535805
Goat anti-Rabbit IgG (H+L) Highly Cross-Adsorbed Secondary Antibody, Alexa Fluor™ 647	Thermo Fisher Scientific	Cat# A-21245; RRID:AB_2535813
Alexa Fluor 488-AffiniPure F(ab')2 Fragment Donkey Anti-Chicken IgY (IgG) (H+L)	Jackson ImmunoResearch Labs	Cat# 703-546-155; RRID:AB_2340376
Alexa Fluor 488-AffiniPure F(ab')2 Fragment Donkey Anti-Rat IgG (H+L)	Jackson ImmunoResearch Labs	Cat# 712-546-150; RRID:AB_2340685
Anti-mouse IgG (H+L), F(ab')2 Fragment (Alexa Fluor® 647 Conjugate)	Cell Signaling Technology	Cat# 4410; RRID:AB_1904023
Anti-mouse IgG (H+L), F(ab')2 Fragment (Alexa Fluor 555 Conjugate)	Cell Signaling Technology	Cat# 4409; RRID:AB_1904022
Anti-mouse IgG (H+L), F(ab) 2 Fragment (Alexa Fluor 488 Conjugate)	Cell Signaling Technology	Cat# 4408; RRID:AB_10694704
Anti-rabbit IgG (H+L), F(ab) 2 Fragment (Alexa Fluor 555 Conjugate)	Cell Signaling Technology	Cat# 4413; RRID:AB_10694110
Goat anti-Rabbit IgG (H+L) Cross-Adsorbed Secondary Antibody, Alexa Fluor™ 750	Thermo Fisher Scientific	Cat# A-21039; RRID:AB_2535710
Peroxidase-AffiniPure Donkey Anti-Mouse IgG (H+L)	Jackson ImmunoResearch Labs	Cat# 715-035-151; RRID:AB_2340771
Peroxidase-AffiniPure Donkey Anti-Rabbit IgG (H+L)	Jackson ImmunoResearch Labs	Cat# 711-035-152; RRID:AB_10015282
Peroxidase-AffiniPure Goat Anti-Rat IgG, Light Chain* Specific	Jackson ImmunoResearch Labs	Cat# 112-035-175; RRID:AB_2338140
Chemicals, peptides, and recombinant proteins		
Tissue-Plus™ O.C.T. Compound	Thermo Fisher Scientific	Cat# 23730571
UltraPure™ Low Melting Point Agarose	Thermo Fisher Scientific	Cat# 16520050
ProLong™ Diamond Antifade Mountant	Thermo Fisher Scientific	Cat# P36961
ProLong™ Glass Antifade Mountant	Thermo Fisher Scientific	Cat# P36980
ProLong™ Gold Antifade Mountant with DAPI	Thermo Fisher Scientific	Cat# P36941
Fluoromount-G™ Mounting Medium	Thermo Fisher Scientific	Cat# 00-4958-02
Normal Goat Serum	Jackson ImmunoResearch Labs	Cat# 005-000-121; RRID: AB_2336990
HBSS, calcium, magnesium, no phenol red	Thermo Fisher Scientific	Cat# 14025076
Dulbecco's Phosphate-Buffered Saline, 10X with calcium and magnesium	Corning	Cat# 20-030-CV
DAPI (4',6-Diamidino-2-Phenylindole, Dilactate)	Thermo Fisher Scientific	Cat# D3571
ActinRed™ 555 ReadyProbes™ Reagent (Rhodamine phalloidin)	Thermo Fisher Scientific	Cat# R37112
EZview™ Red Anti-HA Affinity Gel	Millipore Sigma	Cat# E6779
Pitstop 2	Abcam	Cat# ab120687
Lipofectamine™ 3000 Transfection Reagent	Thermo Fisher Scientific	Cat# L3000001
Doxycycline hyclate	Millipore Sigma	Cat# D5207
EZ-Link Sulfo-NHS-Biotin	Thermo Fisher Scientific	Cat# 21217

REAGENT or RESOURCE	SOURCE	IDENTIFIER
RNAscope™ Probe-Mm-Gli1	ACD	Cat# 311001
Cycloheximide	Millipore Sigma	Cat# 01810
Protein A/G PLUS-Agarose	Santa Cruz	Cat# sc-2003
Critical commercial assays		
DIG RNA Labeling Kit (SP6/T7)	Roche	Cat# 11175025910
ECL™ Prime Western Blotting System	Millipore Sigma	Cat# GERPN2232
RNAscope™ Multiplex Fluorescent Reagent Kit v2	ACD	Cat# 323100
RNeasy Micro Kit	Qiagen	Cat# 74004
TruSeq RNA Library Prep Kit v2	Illumina	Cat# RS-122-2001
Dual-Luciferase Reporter Assay System	Promega	E1960
Deposited data		
Bulk Disp RNA seq	This paper	GEO: GSE242161
Bulk Myo10 RNA seq	This paper	GEO: GSE242161
Experimental models: Cell lines		
Mus musculus: NIH3T3	ATCC	RRID:CVCL_0594
Mus musculus: Neuro-2a	ATCC	RRID:CVCL_0470
Mus musculus: Dispatched KO (DispKO) MEF	Ma et al., Tukachinsky et al.[22,26]	N/A
Mus musculus: DispKO SHH MEF	Stewart et al.[39]	N/A
Mus musculus: MEF wild type	Hall et al.[36]	N/A
Mus musculus: Myo10 KO MEFs	Hall et al.[36]	N/A
Mus musculus: IMCD-3	ATCC	RRID:CVCL_0429
Mus musculus: Light II	ATCC	RRID:CVCL_2721
Canis lupus familiaris: MDCK	ATCC	RRID:CVCL_0422
Experimental models: Organisms/strains		
C57BL/6J (Wild type)	JAX	RRID:IMSR_JAX:00 0664
B6.129(Cg)-Gt(ROSA)26Sortm4$^{(ACTB-tdTomato,-EGFP)Luo}$/J (mT/mG)	JAX	RRID:IMSR_JAX:00 7676
B6.Cg-Shh$^{tm1(EGFP/cre)Cjt}$/J	JAX	RRID:IMSR_JAX:00 5622
B6.129X1(Cg)-Shh^{tm6Amc}/J	JAX	RRID:IMSR_JAX:00 8466
B6.Cg-Myo10^{m1J}/GrsrJ	JAX	RRID:IMSR_JAX:02 4583
C57BL/6-Disp1$^{INDEL/+}$	This paper	N/A
C57BL/6-Disp1$^{CS/+}$	This paper	N/A
Oligonucleotides		
CRISPR-Cas9 editing constructs (see Table S1)	This paper	N/A
DISP1 editing constructs (see Table S1)	This paper	N/A
Recombinant DNA		
pcDNA3.1(+) (control vector)	Thermo Fisher Scientific	Cat# V79020
pCDNA3-EGFP	A gift from Doug Golenbock	RRID:Addgene_13031
pCMV-mCherry-Membrane	Yost et al.[98]	RRID:Addgene_55779

REAGENT or RESOURCE	SOURCE	IDENTIFIER
pCMV-R-GECO1	Zhao et al[99]	RRID:Addgene_32444
pCMV-mCherry2	A gift from Michael Davidson	RRID:Addgene_54517
pCDNA3.1-mSHH-FL	Stewart et al.[39]	N/A
pCDNA3.1-mSHH-FL-EGFP	Hall et al.[36]	N/A
pCDNA3.1-V5-DISPWT-HA	Stewart et al.[39]	RRID:Addgene_126410
pCDNA3.1-V5-DISPCS-HA	Stewart et al. [39]	N/A
pCDNA3.1-V5-DISPΔC-HA	This paper	N/A
pCDNA3.1-V5-DISP4xAA-HA	This paper	N/A
pCDNA3.1-V5-DISPWT-Dronpa3-HA	This paper	N/A
pCDNA3.1-V5-DISPCS-Dronpa3-HA	This paper	N/A
pCDNA3.1-DISP ΔC-Dronpa3-HA	This paper	N/A
Dronpa3-N1	A gift from Michael Davidson	RRID:Addgene_54682
pLVX-Tet-On 3G	Takara	Cat# 631187
pCMV3-hBMP2-GFPSpark	Sino Biological	Cat# HG10426-ACG
pCMV3-hBMP4-OFPSpark	Sino Biological	Cat# HG10609-ACR
pCMV3-hBMP7-GFPSpark	Sino Biological	Cat# HG10083-ACG
pCMV3-hWNT1-GFPSpark	Sino Biological	Cat# HG10721-ACG
Software and algorithms		
Fiji (ImageJ) (v2.9.0)	Schindelin et al. [91] RRID:SCR_002285	http://fiji.sc
CellProfiler (v4.2.5)	McQuin et al. [102] RRID:SCR_007358	http://cellprofiler.org
Ilastik (v1.4.0)	Berg et al. [95] RRID:SCR_015246	http://ilastik.org/
CATMAID (v2021.12.20)	Saalfeld et al., Schneider-Mizell et al. [72,97] RRID:SCR_006278	http://catmaid.org/
CRIS.py (v2.0)	Connelly et al.[87]	https://github.com/patrickc01/CRIS.py
Leica Application Suite X (LAS X) (v4.0.0)	Leica RRID:SCR_013673	https://www.leica-microsystems.com/products/microscope-software/details/product/leica-las-x-ls/
NIS Elements (v5.41.02)	Nikon RRID:SCR_014329	https://www.nikoninstruments.com/Products/Software
GraphPad Prism (v8.0)	GraphPad RRID:SCR_002798	http://www.graphpad.com/
Amira (v2020.3)	ThermoFisher RRID:SCR_007353	http://www.fei.com/software/amira-3d-for-life-sciences/
Inveon Research Workplace (v3.0)	Siemens	https://inveon-research-workplace.software.informer.com/
Molecular Signatures Database (GSEA) (v2023.1.Mm)	Subramanian et al. [96] RRID:SCR_016863	http://software.broadinstitute.org/gsea/msigdb/index.jsp

REAGENT or RESOURCE	SOURCE	IDENTIFIER
Photoshop (v24.3)	Adobe RRID:SCR_014199	https://www.adobe.com/products/photoshop.html
Illustrator (v27.4.1)	Adobe RRID:SCR_010279	http://www.adobe.com/products/illustrator.html
Premiere Pro (v15.4.1)	Adobe RRID:SCR_021315	https://www.adobe.com/products/premiere.html
CLC Genomics Server (v23.0.4)	Qiagen RRID:SCR_017396	https://www.qiagenbioinformatics.com/products/clc-genomics-server/
Partek Genomics Suite (v7.0)	Partek Inc. RRID:SCR_011860	http://www.partek.com/?q=partekgs